Avalanche criticality in individuals, fluid intelligence and working memory

Longzhou Xu [a, 1], Lianchun Yu [a, b, 1, *], Jianfeng Feng [c, d, e, **]

[a] School of Physical Science and Technology, and Key Laboratory for Magnetism and Magnetic Materials of MOE, Lanzhou University, Lanzhou, 730000, China

[b] The School of Nationalities' Educators, Qinghai Normal University, Xining, 810000, China

[c] Institute of Science and Technology for Brain Inspired Intelligence, Fudan University, Shanghai, 200433, China

[d] Department of Computer Science, University of Warwick, Coventry, CV4 7AL, UK

[e] School of Mathematical Sciences, School of Life Science and the Collaborative Innovation Center for Brain Science, Fudan University, Shanghai, 200433, PR China

[*] Corresponding author. School of Physical Science and Technology, and Key Laboratory for Magnetism and Magnetic Materials of MOE, Lanzhou University, Lanzhou, 730000, China

[**] Corresponding author. Institute of Science and Technology for Brain Inspired Intelligence, Fudan University, Shanghai, 200433, China

[1] These authors contributed equally to this work.

E-mail addresses: xulzh18@lzu.edu.cn (L. Xu); yulch@lzu.edu.cn (L. Yu); Jianfeng.Feng@warwick.ac.uk (J. Feng).

Abstract

The critical brain hypothesis suggests that efficient neural computation can be realized by dynamics of the brain characterized by a scale-free avalanche activity. However, to pursue this hypothesis requires not only accurately identifying the critical point but also analyzing the phase transition in brains so that different cognitive states could be mapped. In this work, we analyzed the mean synchronization and synchronization entropy of blood oxygenation level signals from resting-state fMRI. We found that the scale-free avalanche activity associated with intermediate synchrony and maximal variability of synchrony. We verified that the complexity of the functional connectivity, in addition to the coupling between structural and functional networks, was maximized at criticality. We observed order-disorder phase transitions in resting-state brain dynamics and found that there were longer times spent in the subcritical regime. These results support the hypothesis that large-scale brain networks lie in the vicinity of a critical point. The critical dynamics observed were associated with high scores in fluid intelligence and working memory tests but were not crystallized intelligence scores. We identified brain regions whose critical dynamics showed significant positive correlation with fluid intelligence performance, and found these regions were located in the frontal cortex, superior parietal lobule, angular gyrus and supramarginal gyrus which are believed to be important nodes of brain networks underlying human intelligence. Our results reveal the role that avalanche criticality plays in cognitive performance, and provide a simple method to map cortical states on a spectrum of neural dynamics and capture the phase transition, with a critical point in the domain.

1. Introduction

The critical brain hypothesis states that the brain operates in close vicinity to a critical point that lies between order and disorder. This is characterized by a power-law form of the event size distribution (Cocchi et al., 2017; Hesse and Gross, 2014). This hypothesis is supported by a set of observations of power-law scaling in many different neural systems using various approaches (Beggs and Plenz, 2003; Gal and Marom, 2013; Meisel et al., 2013; Plenz, 2012; Shriki et al., 2013; Solovey et al., 2012; Tagliazucchi et al., 2012). Arguments in favour of this hypothesis have been strengthened by advantages in information transmission, information storage, and dynamic range, in neural systems operating near criticality (Shew et al., 2009; Shew et al., 2011; Yang et al., 2012), with evidence arising in both theoretical and experimental work (Shew and Plenz, 2012). Meanwhile, this hypothesis still faces challenges from several perspectives (Beggs and Timme, 2012). For example, computational studies suggested that power laws may emerge from simple stochastic processes or noncritical neuronal systems (Touboul and Destexhe, 2010), so power law alone are prerequisite but not sufficient evidence for criticality. Meanwhile, it has been asked: “If the brain is critical, what is the phase transition (Fontenele et al., 2019)?” Indeed, the observation of power law avalanche activity along with a phase transition between order and disorder would be more persuasive for criticality. Furthermore, though previous studies have associated supercriticality with reduced consciousness (Meisel et al., 2013; Scott et al., 2014), near-critical dynamics with rest (Priesemann et al., 2014), and subcriticality with focused cognitive states (Fagerholm et al., 2015), there remains a gap between the specific brain state and efficient information processing endowed by criticality as predicted by theory (He, 2011). To fully understand the functional roles of critical and non-critical dynamics, more research is required to relate brain states and cognitive performance to neural dynamics that lie on a spectrum, ranging from subcriticality to supercriticality. To obtain a deeper understanding of this phenomenon, it is necessary to develop data analysis methods to represent this phase spectrum with high resolution and characterize the subsequent reorganization of brains with the transition in this spectrum (Fontenele et al., 2019).

With advances in brain imaging techniques such as functional magnetic resonance imaging (fMRI), the critical brain hypothesis has found roles in interpreting fundamental properties of large-scale brain networks in the context of structure-dynamics-function relationships (Karahanoğlu and Van De Ville, 2017; Lee et al., 2019). For example, it has been shown that structural connections of brains are mostly reflected in functional networks, and this structure-function coupling is disrupted when brains move away from criticality during anesthesia (Tagliazucchi et al., 2016). Another application of criticality is to explain the dynamic basis of brain complexity (Popiel, 2020; Tagliazucchi and Chialvo, 2013; Timme et al., 2016). In particular, functional connectivity (FC) complexity, which is an umbrella term describing the variability, diversity, or flexibility of functional connections in brain networks, has been associated with cognitive performance from many perspectives, such as high-order cognition, aging, and cognitive impairment in brain disorders (Ahmadlou et al., 2014; Anokhin et al., 1996; Omidvarnia et al., 2019; Smyser et al., 2016; Wang et al., 2017). Studies have suggested that the FC complexity may possibly be at its maximum at the critical point, while the FC capacity arises from special topological properties of the structural network, such as hierarchical modular organization (Song et al., 2019; Wang et al., 2019).

To validate these applications, both computer modeling methods and experimental data analysis methods were used. Computer modeling utilizes structural imaging data to model large-scale brain dynamics and functional networks (Deco et al., 2011; Nakagawa et al., 2013). However, there is still disagreement on which type of phase transition should be adopted for large-scale brain networks, e.g., first-order discontinuous vs. second-order continuous phase transitions and edge of chaos criticality vs. avalanche criticality (Kanders et al., 2017; Scarpetta et al., 2018). Experimental studies usually take advantage of dynamic changes caused by interventions, such as deprived sleep, anesthesia, or brain diseases, to show deviations from criticality and subsequent reorganization of FC networks (Hobbs et al., 2010; Meisel et al., 2013; Meisel et al., 2012; Tagliazucchi et al., 2016). However, deviations caused by these interventions are usually unidirectional, either in the sub- or supercritical directions. Furthermore, it is not clear whether deviations from criticality caused by different intervention methods follow an identical phase

transition trajectory. Recent studies have proposed the concept of a “critical line” instead of a “critical point” and suggested that multiple phase transition trajectories may exist (Kanders et al., 2020). Therefore, the successful recovery of the phase transition trajectory from a large-scale brain network will not only help to answer key questions regarding what the phase transition is if the brain is critical but also have important implications in brain functional imaging and large-scale brain modeling.

In this study we focused on the mean synchronization (MS) of blood oxygenation level-dependent (BOLD) signals versus their synchronization entropy (SE), as obtained from resting-state fMRI (rfMRI) scanning. We used such signals to identify the critical point and phase transition in large-scale brain networks. The inverted-U trajectory for MS vs. SE, which was first reported by Yang et al (Yang et al., 2012). These authors found in a computer model with balanced excitation-inhibition (E-I) that a moderate mean value in synchrony with high variability emerged at the critical point. They also demonstrated this fact in rat cortex slice culture with drug-induced E-I imbalance and loss of criticality. Later, Meisel et al. used electroencephalography (EEG) recordings to find increased MS with decreased SE as brains shift from the critical point toward a supercritical regime during prolonged wakefulness (Meisel et al., 2013). These studies anticipated that a moderate mean in synchrony, with maximal variability, might be associated with criticality that exists at different levels of neural systems. We characterized the resting brain state of individual subjects by a point in the MS vs. SE phase plane. These points were found to produce an inverted-U phase-trajectory, which previous work (Meisel et al., 2013; Yang et al., 2012) suggested represents an order-disorder phase transition in large-scale brain networks.

We then used an avalanche distribution analysis (Beggs and Plenz, 2003; Tagliazucchi et al., 2012) to confirm that the tipping point of this inverted-U curve was closest to the criticality, which separates ordered/supercritical and disordered/subcritical regimes. Based on the above, we further examined previous conjectures on criticality in large-scale brain networks and found that both FC complexity and structure-function coupling were maximized around the criticality. We utilized a sliding window approach to observed that an “instantaneous” phase transition occurred

in individual brains. We showed that brains persisting in the subcritical regime exhibited longer dwell times than those in other regimes. Finally, we found that subjects whose brains were closer to the criticality yielded high scores in fluid intelligence and working memory tests. Additionally, the critical dynamics in the frontal cortex, superior parietal lobule, angular gyrus and supramarginal gyrus et al, which were believed as vital regions in the networks of Parieto-Frontal Integration Theory (P-FIT) for intelligence (Jung and Haier, 2007), showed significant correlations with fluid intelligence performance.

2. Material and methods

2.1 Data acquisition and preprocessing

2.1.1. fMRI data acquisition and preprocessing

We used rfMRI data from the Human Connectome Project (HCP) 1200-subject release (Van Essen et al., 2013). Each subject underwent two sessions of rfMRI on separate days, each session with two separate 14 min 24s acquisitions generating 1200 volumes on a customized Siemens 3T Skyra scanner ($\mathrm{TR} = 720\ \mathrm{ms}$, $\mathrm{TE} = 33\ \mathrm{ms}$, flip angle $= 52\,°$, voxel size $= 2$ mm isotropic, 72 slices, $\mathrm{FOV} = 208 \times 180\mathrm{mm}$, matrix $= 104 \times 90$ mm, multiband accelaration factor $= 8$, echo spacing $= 0.58\ \mathrm{ms}$). The rfMRI data used for our analysis were processed according to the HCP minimal preprocessing pipeline (Glasser et al., 2016; Glasser et al., 2013) and denoising procedures. The denoising procedure pairs the independent component analysis with the FSL tool FIX to remove non-neural spatiotemporal components (Smith et al., 2015). And as a part of cleanup, HCP used 24 confound timeseries derived from the motion estimation (the 6 rigid-body parameter timeseries, their backwards-look temporal derivatives, plus all 12 resulting regressors squared). Note that the global component of the fMRI fluctuations measured during the resting state is tightly coupled with the underlying neural activity, and the use of global signal regression as a pre-processing step in resting-state fMRI analyses remains controversial and is not universally recommended (Liu et al., 2017). Therefore, the global whole-brain signal was not removed in this work. We used the left-to-right acquisitions from the first resting-state dataset

(i.e., resting state fMRI 1 FIX-denoised package).

The first 324 subjects in the dataset entered into our study, and we excluded 29 subjects for missing data. This left us with 295 subjects for further analysis, and 162 of them were females. All the participants were between the ages of 22-36, 58 were between the ages of 22-25, 130 were between the ages of 26-30, 104 were between the ages of 31-35, and 3 were 36 years old.

For further analysis, the whole cortex was parcellated into 96 regions (Makris et al., 2006), and the details are provided at https://identifiers.org/neurovault.image:1699, and from each region the time series averaged across the voxels were extracted and Z-normalized to construct region of interest (ROI) signals ($atlas_{96}$ signals). To test the results for different parcellation, we also used the Human Brainnetome atlas (the whole brain was parcellated into 246 regions with Human Brainnetome Atlas, which contains 210 cortical and 36 subcortical regions (Fan et al., 2016), the details are provided at http://atlas.brainnetome.org/bnatlas.html) and Zalesky 1024 regions (Zalesky et al., 2010), the resulting signals were termed as $atlas_{246}$ and $atlas_{1024}$ signals, respectively.

2.1.2. Diffusion tensor imaging (DTI) data acquisition and preprocessing

The diffusion MRI images used in this study were also from the HCP 1200-subject release (Sotiropoulos et al., 2013). Briefly, the diffusion data were collected using a single-shot, single refocusing spin-echo, echo-planar imaging sequence ($\mathrm{TR} = 5520\ \mathrm{ms}$, $\mathrm{TE} = 89.5\ \mathrm{ms}$, $\text{flip angle} = 78°$, $\mathrm{FOV} = 210 \times 180\ \mathrm{mm}$, $\text{matrix} = 168 \times 144\ \mathrm{mm}$, $\text{voxel size} = 1.25\ \mathrm{mm}$ istropic, $\text{slices} = 111$, multiband acceleration factor $= 3$, echo spacing $= 0.78\ \mathrm{ms}$). Three gradient tables of 90 diffusion-weighted directions and six b=0 images each, were collected with right-to-left and left-to-right phase encoding polarities for each of the three diffusion weightings (b=1000, 2000, and 3000 s/mm^2). All diffusion data were preprocessed with the HCP diffusion pipeline updated with EDDY 5.0.10 (Sotiropoulos et al., 2013), and the details are provided at https://www.humanconnectome.org. In this study, from the 295 selected subjects, only 284 subjects were entered into our DTI data analysis because 11 of them were missing the corresponding DTI data.

2.1.3. Cognition measures

We examined associations between intelligence and critical dynamics conducted in our rfMRI analysis. Three relevant behavioral tasks were used as a measure of cognitive ability, including fluid intelligence, working memory, and crystallized intelligence. The same 295 subjects were also entered into our cognitive ability analysis, but for the fluid intelligence analysis, 4 subjects were excluded due to missing intelligence scores.

The fluid intelligence scores in the HCP data release were measured using the number of correct responses on form A of the Penn Matrix Reasoning Test (PMAT, $\text{mean} = 17.01$, $\text{standard deviation (SD)} = 4.91$, $\text{range} = 4 - 24$) (Barch et al., 2013; Hearne et al., 2016), which had 24 items and 3 bonus items, using nonverbal visual geometric designs with pieces to assess reasoning abilities that can be administered in under 10 min (Barch et al., 2013; Hearne et al., 2016). The PMAT (Bilker et al., 2012) is an abbreviated version of Raven's Standard Progressive Matrices test (Wendelken et al., 2007), which comprises 60 items.

Crystallized intelligence was measured using the picture vocabulary test from the National Institutes of Health (NIH) toolbox (Barch et al., 2013; Hearne et al., 2016). This measure of receptive vocabulary was administered in a computer-adaptive testing (CAT) format. The participant was presented with four pictures and heard an audio recording saying a word, and was instructed to select the picture that most closely showed the meaning of the word. Because the test used a variable length CAT with a maximum of twenty-five items, some participants had fewer items, and the presented words depended on the participant's performance. Raw scores were converted to age-adjusted scores. Here, we used the unadjusted scores (Picture vocabulary, mean=116.9, SD=10.16, range=92.39-153.09).

Working memory was assessed using the List Sorting Working Memory test from the NIH Toolbox (Barch et al., 2013), in which the participants were required to sequence sets of visually and a small number of orally presented stimuli in size order from smallest to biggest. Pictures of different foods and animals were displayed with both a sound clip and a written test that names them, and involved two different conditions. In the 1-list condition, participants ordered a series

of objects, either food or animals, but in the 2-list condition, participants were presented with both animal and food lists and asked to order each list by increasing size. The number of list items increased in subsequent trials, and the task was discontinued after 2 consecutive incorrect trials. Raw scores were the sum of the total correct items, which were converted to age-adjusted scores. Here, we used the unadjusted scores (List sorting, mean=111.13, SD=12.02, range=84.83-144.50).

2.2. Methods

2.2.1. Synchrony and variability in synchrony

We measured the mean and variability in synchronization with a previously described approach (Meisel et al., 2013; Yang et al., 2012). First, we obtained the phase trace $\theta_j(t)$ from the signal $F_j(t)$ using its Hilbert transform $H[F_j(t)]$:

$$\theta_j(t) = arctan\frac{H[F_j(t)]}{F_j(t)}. \quad (1)$$

Next, we calculated the Kuramoto order parameter as follows:

$$r(t) = \frac{1}{u}\left|\sum_{j=1}^{u} e^{i\theta_j(t)}\right|, \quad (2)$$

in which u is the number of ROIs in global network analysis or is the number of voxels in a particular region in regional analysis. The Kuramoto order parameter $r(t)$ was used as a time-dependent measure of phase synchrony of a system. The MS in a time period was calculated as

$$\langle r \rangle = \frac{1}{V}\sum_{t=1}^{V} r(t), \quad (3)$$

where V is the length of the time period. In this study, we calculated static MS in the entire scan period with $V = 1200$ time points. We derived the entropy of $r(t)$ as the measure of variability in synchronization (synchronization entropy, SE):

$$H(r) = -\sum_{n=1}^{N} p_n \, log_2 \, p_n, \quad (4)$$

where p_n is the probability that $r(t)$ falls into a bin between $min\,(r(t)) \leq b_n < r(t) < b_{n+1} \leq max\,(r(t))$. In this study, we chose the number of bins $N = 30$, and the robustness of our results was also tested with an interval between 5 and 100.

2.2.2. Avalanche analysis

In our avalanche analysis, the ROI signals were reduced to a spatiotemporal point process by detecting the suprathreshold peak positions intermediate between two above-threshold time points, as shown in the example of Fig. 1 **a**. By binning the binary sequences with appropriate time resolution (time bin), we obtained a spatial pattern of active ROIs within consecutive time bins. An avalanche was defined as a series of consecutively active bins, which were led and followed by blank bins without activations. The size S and duration T of the avalanches were then defined as the total number of activations and total number of time bins during this avalanche, respectively (Beggs and Plenz, 2003; Tagliazucchi et al., 2012).

If a system operates near a critical point, the size distribution ($P(S)$), duration distribution ($P(T)$), and average size for a given duration ($\langle S \rangle(T)$) should be fitted into power laws:

$$P(S) \sim T^{-\alpha}, \tag{5}$$

$$P(T) \sim T^{-\tau}, \tag{6}$$

$$\langle S \rangle(T) \sim T^{\gamma}, \tag{7}$$

where α, τ, and γ are critical exponents of the system (Friedman et al., 2012; Sethna et al., 2001). Furthermore, the following relationship was proposed as an important evaluation of the critical system (Fontenele et al., 2019; Friedman et al., 2012), namely,

$$\frac{\tau-1}{\alpha-1} = \gamma. \tag{8}$$

In this study, we defined

$$\delta = \left|\frac{\tau-1}{\alpha-1} - \gamma\right| \tag{9}$$

to measure the distances of the systems from the critical point, so the smaller δ is, the closer the

systems are to the critical point.

The scaling exponents governing the power-law distribution were estimated using the maximum likelihood estimator (MLE) (Clauset et al., 2009; Marshall et al., 2016). Briefly, the MLE procedure supposed that the empirical data sample was from a power-law function in the range (x_{min}, x_{max}), with probability density $\frac{1}{\sum_{x=x_{min}}^{x_{max}} (\frac{1}{x})^{\alpha}} \left(\frac{1}{x}\right)^{\alpha}$ (Fontenele et al., 2019; Marshall et al., 2016). We estimated critical exponents α and τ by maximizing the likelihood function and via a lattice search algorithm (Marshall et al., 2016). We then used Clauset's goodness-of-fit test to quantify the plausibility of fits (Clauset et al., 2009; Deluca and Corral, 2013; Marshall et al., 2016). We used a power-law model to produce data sets over the fit range and compared the Kolmogorov–Smirnov (KS) statistics between (1) the real data and the fit against (2) the model data and the fit. If the real data produced a KS-statistic that was less than the KS-statistic found for at least 10% of the power-law models (i.e., $p \geq 0.1$), we accepted the data as being fit by the truncated power law because the fluctuations of the real data from the power law were similar in the KS sense to random fluctuation in a perfect power-law model.

2.2.3. surrogate data

To assess the statistical significance of the avalanche analysis results and MS-SE relationship, we generated comparable surrogate data and applied the analyses above to these data. Phase-shuffling is often used in hypothesis testing for avalanche size distribution(Gireesh and Plenz, 2008; Shriki et al., 2013). Phase-shuffling disrupts temporal as well as spatial correlations in multichannel time series.

Herein phase shuffling was done on the $atlas_{96}$ signals. The phase randomization procedures were as follows (Prichard and Theiler, 1994): (1) the discrete Fourier transformations was taken to of each subject; (2) rotate the phase at each frequency by an independent random variable that was uniformly chosen in the range $[0,2\pi]$. Crucially, the different time series were rotated by the different phases to randomize the phase information; (3) the inverse discrete Fourier transformation was applied to these time series to yield surrogate data.

2.2.4. Branching parameter

The branching parameter σ, which is defined as the average number of subsequent events that a single preceding event in an avalanche triggers, is a convenient measure to identify criticality (Beggs and Plenz, 2003). In theory, the system is critical for $\sigma = 1$ and sub- (super) critical for $\sigma < 1$ ($\sigma > 1$). In this study, σ was calculated as

$$\sigma = \frac{1}{N}\sum_{i=1}^{N}\frac{n_i^*}{n_i}, \tag{10}$$

where n_i is the number of ancestors, n_i^* is the number of descendants in the next time bin, and N is the total number of time bins with activations.

2.2.5. Definition of kappa

A nonparametric measure, κ, for neuronal avalanches was introduced by Shew and his colleagues (Shew et al., 2009). It quantifies the difference between an experimental cumulative density function (CDF) of the avalanche size, $F(\beta_k)$, and the theoretical reference CDF, $F^{NA}(\beta_k)$, which is a power-law function with theoretical expected exponent $\alpha = 1.5$:

$$\kappa = 1 + \frac{1}{m}\sum_{k=1}^{m}\left(F^{NA}(\beta_k) - F(\beta_k)\right), \tag{11}$$

where β_k are avalanche sizes logarithmically spaced between the minimum and maximum observed avalanche sizes, and m is the number of histogram bins. The unit value of κ is characteristic of the system in a critical state, whereas values below and above 1 suggest sub- and supercritical states, respectively.

2.2.6. Functional and structure connectivity matrix

We constructed an FC matrix from atlas$_{96}$ signals by computing the Pearson correlation C_{ij} between ROI i and ROI j, and the mean FC strength $\langle FC \rangle$ was obtained by

$$\langle FC \rangle = \langle |C_{ij}| \rangle, \tag{12}$$

where $|\cdot|$ means the absolute value.

The structure connectivity (SC) matrix was constructed using DSI Studio (http://dsi-studio.labsolver.org) from DTI data. The DTI data were reconstructed in the Montreal Neurological Institute (MNI) space using q-space diffeomorphic reconstruction (Yeh and Tseng, 2011) to obtain the spin distribution function (Yeh et al., 2010). A diffusion sampling length ratio of 1.25 was used. The restricted diffusion was quantified using restricted diffusion imaging (Yeh et al., 2017), and a deterministic fiber tracking algorithm (Yeh et al., 2013) was used to obtain one million fibers with whole-brain seeding. The angular threshold was randomly selected from 15 degrees to 90 degrees. The step size was randomly selected from 0.1 voxels to 3 voxels. The anisotropy threshold was automatically determined by DSI Studio. The fiber trajectories were smoothed by averaging the propagation direction with a percentage of the previous direction. The percentage was randomly selected from 0% to 95%. Tracks with a length shorter than 5 or longer than 300 mm were discarded. The 96-regions atlas was used, and the SC matrix was calculated by using the count of the connecting tracks.

2.2.7. Functional connectivity entropy

The FC entropy, $H(FC)$, used in this study was similar to the early work of Yao et al. (Yao et al., 2013), which is calculated by

$$H(FC) = \sum_i - p_i log_2(p_i), \tag{13}$$

where p_i is the probability distribution of $|C_{ij}|$, i.e., $\sum_i p_i = 1$. In the calculation, the probability distribution was obtained by discretizing the interval (0, 1) into 30 bins.

2.2.8. Functional connectivity diversity

As defined in the recent work of Wang et al (Wang et al., 2019), the functional diversity ($D(FC)$) of the FC matrix is measured by the similarity of the distribution to the uniform distribution:

$$D(FC) = 1 - \frac{1}{N_M} \sum_{i=1}^{M} \left| p_i - \frac{1}{M} \right|, \tag{14}$$

where $N_M = 2\frac{M-1}{M}$ is a normalization factor, $D(FC)$ is in the range [0, 1], and p_i is the

probability distribution of $|C_{ij}|$, which was obtained by discretizing the interval (0, 1) into M bins ($M = 30$ in this work). For completely asynchronous or synchronized states, the correlation values fall in one bin at 0 or 1, where $D(FC) = 0$ reflects the simple dynamic interaction pattern. In an extreme case where all types of FC equivalently exist, p_i would ideally follow a uniform distribution (i.e., probability in each bin $= \frac{1}{M}$) and $D(FC) = 1$.

2.2.9. Functional connectivity flexibility

Similar as previous works, to obtain the flexibility of FC among whole brain, we utilized the sliding window method to calculate connectivity number entropy (CNE) for each region (Lei et al., 2020; Song et al., 2019). A non-overlapping sliding window method was applied to the atlas$_{96}$ signals. The choice of window size must be sufficient to yield a stable Pearson's correlation coefficient within each window, yet small enough to reveal the temporal-dependent variation in FC (Lei et al., 2020; Sakoğlu et al., 2010). We chose a window size in the range of 20-30, corresponding to the number of windows (n_{win}) in the range of 40-60.

Within each time window, we first acquired the FC matrix via their time series in this window. Then, the binary network matrix was obtained by binarizing the FC matrix with threshold THR_{FC}. Subsequently, we calculated the number of regions connected to a particular region k ($k = 1, 2, \ldots 96$) in each time window. Therefore, we could obtain p_i, the probability for a particular connection number occurring, where i indicated the i-th connection number among all possible connection numbers. Then, CNE for the region k is a complexity measure (i.e., Shannon entropy) for the disorder in the connection numbers over time:

$$CNE_k = -\sum_{i=1}^{95} p_i log_2 p_i, \tag{15}$$

where the summation index runs from 1 to the number of all possible connection numbers.

For each subject, the CNE at the whole-brain level was obtained by simply averaging the regional CNE_k values over 96 regions:

$$CNE = \frac{1}{96}\sum_{k=1}^{96} CNE_k. \tag{16}$$

2.2.10. Similarity between functional and structural networks

To measure the similarity between functional and structural connection networks, the FC matrices C_{ij} were thresholded by THR_{FC} to yield binary adjacency matrices A_{ij} such that $A_{ij} = 1$ if $C_{ij} \geq THR_{FC}$, and $A_{ij} = 0$ otherwise. The parameter THR_{FC} was chosen to fix link density ρ_{FC}, which was defined as the ratio of the connections in the network ($\sum_{i>j} A_{ij}$) to the total possible number of connections. It is important to fix the link density when comparing networks, as otherwise, differences could arise because the average of the respective C_{ij} are different (and therefore the number of nonzero entries in A_{ij}) but not because connections are topologically reorganized across conditions (Tagliazucchi et al., 2016).

The binary FC networks for each subject were compared with the group-aggregated binary SC network but not the individual's SC network to avoid fluctuations in individual SC networks. First, the binary adjacency matrices B_{ij} of SC matrices were obtained for each subject such that $B_{ij} = 1$ if there were tracked fiber links; otherwise, $B_{ij} = 0$. Then, the binary adjacency structural connection matrices were summed up and again thresholded by a thresholding value THR_{SC} to yield a group-aggregated binary SC network. In this way, high THR_{SC} values would exclude connections that were shared by fewer subjects but preserve connections that were common in most subjects.

To estimate the similarity between the binary FC network of each subject and the group-aggregated binary SC network, we computed the Pearson correlation $R(FC - SC)$ and Hamming distance $HD(FC - SC)$ between these two networks (Tagliazucchi et al., 2016). Specifically, the Hamming distance is defined as the number of symbol substitutions (in this case 0 or 1) needed to transform one sequence into another and vice versa, and in this case, it is equal to the number of connections that must be rewired to turn the functional network connection into the structural network connection.

2.2.11. Dynamic analysis of phase transitions

We used the sliding window approach to capture the time-dependent changes in measures used in this study. In the calculation, for the atlas$_{96}$ signals, the length of the sliding window was set to $V = 200$ (volumes), and the sliding step was set to $\Delta n = 10$ (volumes). In each window, we calculated the corresponding dynamic measures, including dynamic MS $\langle r \rangle_n$, dynamic SE $H(r)_n$, and dynamic FC matrix $\left(C_{ij}\right)_n$. From the dynamic FC matrix $\left(C_{ij}\right)_n$, we further obtained dynamic FC entropy $H(FC)_n$, FC diversity $D(FC)_n$, Pearson correlation between FC and SC $\mathrm{R(FC-SC)_n}$, and Hamming distance $HD(FC-SC)_n$.

3. Results

3.1. The signature of critical dynamics in the cortical network

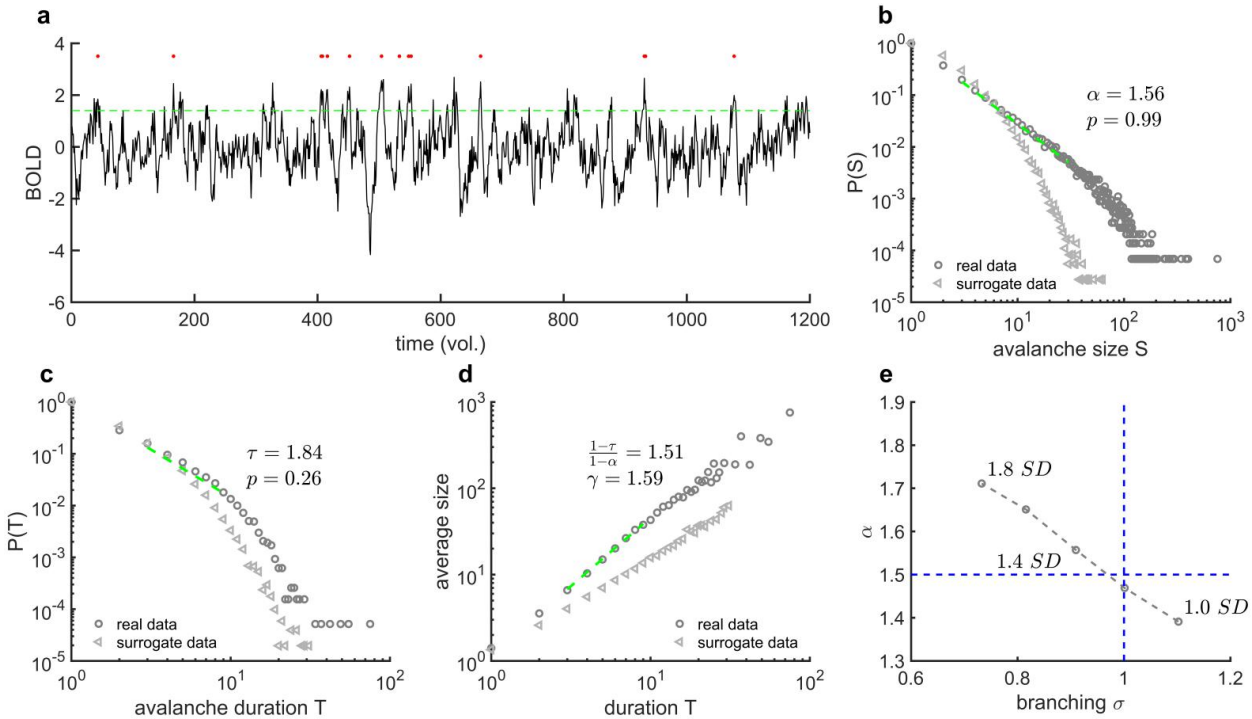

Figure 1 Power-law distribution for the aggregate level reflecting the brain near criticality in the resting state. a Example of a point process (red filled circles) extracted from one

normalized ROI BOLD signal. **b** The probability distributions of group-aggregate avalanche sizes for the 1.4 SD thresholds and a time bin width of 1 volume (vol.) in the fMRI data. The distributions are well approximated by power law with an exponent $\alpha = 1.56$ with Clauset's test $p = 0.99$, corresponding to $\kappa = 0.9912$ (histogram bins=40) and branching parameter $\sigma = 0.9097$. **c** The distribution of avalanche durations for the group-aggregated level can be fit well by a power law with an exponent $\tau = 1.84$ under the condition described in **b**, with Clauset's test $p = 0.26$. **d** There is a power-law relationship between the sizes and duration of the avalanches with a positive index $\gamma = 1.59$, which is close to $\frac{1-\tau}{1-\alpha} = 1.51$. In **b-d**, the grey triangles were calculated from the surrogate data. **e** The branching ratio and power-law scaling exponents α of avalanche sizes for different thresholds used to define the point process.

For the 295 available subjects, we first investigated the power-law distribution of avalanche size at the population level. Here we defined the activation as the time point when the BOLD signals reached their peak value, while the signals one step before and after this time point were above the chosen threshold (Fig. 1 **a**). After preprocessing, the $atlas_{96}$ signals were converted into point processes in which each time point represented an activation. We then calculated the avalanche size distribution $P(S) \sim S^{-\alpha}$ (Fig. 1 **b**), as well as the avalanche duration distribution $P(T) \sim T^{-\tau}$ (Fig. 1 **c**). First, from the estimated α and τ values, we tested whether the relationship between the scaling exponents holds for different thresholds of ROI signals (Fontenele et al., 2019; Friedman et al., 2012). We found that the closest matching occurred when the chosen threshold was around 1.4 SD (Fig. 1 **d**). Second, the power-law distribution of avalanche sizes with a slope of $\alpha = 1.5$ could be predicted by theory for a critical branching process with branching parameter $\sigma = 1$ (Harris, 1964; Zapperi et al., 1995). However, we found that the threshold of 1.4 SD yielded $\sigma = 0.91$ and $\alpha = 1.56$ (Fig. 1 **e**), which did not match well with the theoretical prediction. We ran the same analysis on both $atlas_{246}$ signals (Fig. S1 **a**) and $atlas_{1024}$ signals (Fig. S1 **b**) to find the mismatch still exist (Fig. S1 **c** and **d**).

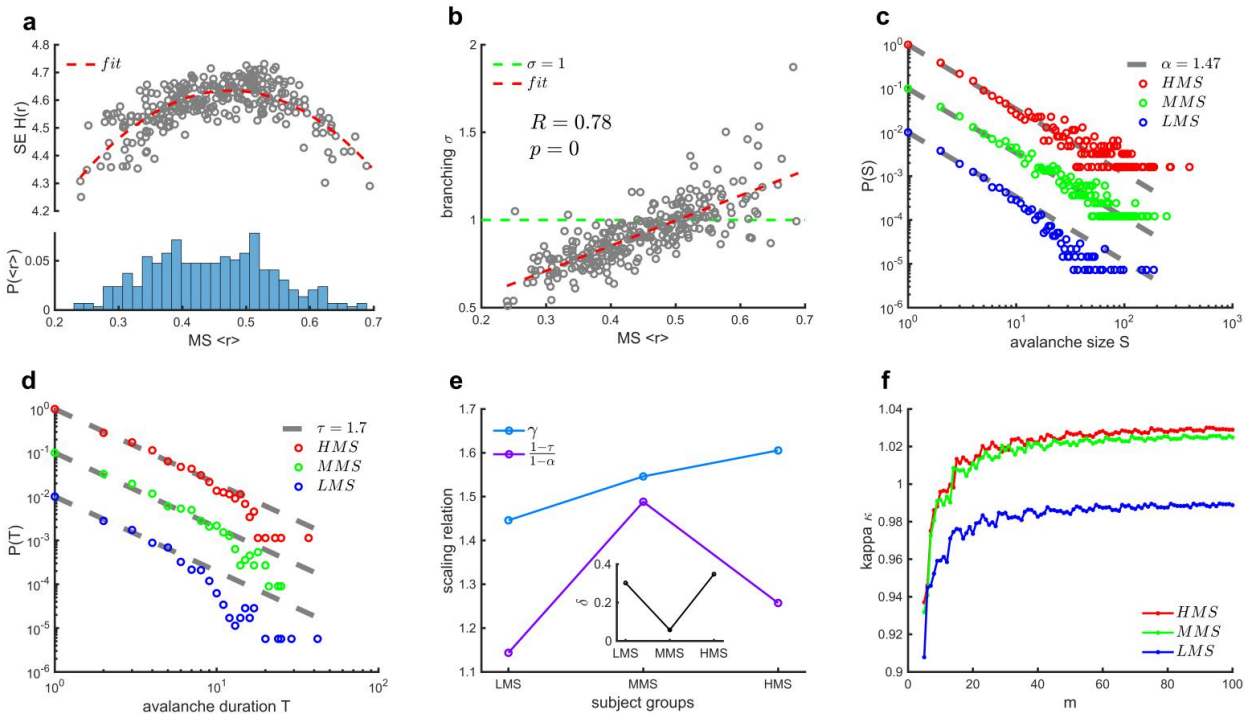

Figure 2 Signatures of criticality as a function of MS in resting-state brain networks. a Top panel: The inverted-U trajectory of the MS $\langle r \rangle$ vs. SE $H(r)$. The line represents the significant quadratic fit of the data (F=188.758 , p<0.001 , adjusted R^2=0.561). Bottom panel: The frequency count for the distribution of MS $\langle r \rangle$. **b** The branching parameters σ vs. $\langle r \rangle$ for each subject. The green dashed line indicates $\sigma = 1$. The Pearson correlation value R and the p value are shown in the figure. The solid line is the linear regression. **c** Avalanche size distributions for the LMS group ($\langle r \rangle = 0.2824 \pm 0.0219$), MMS group ($\langle r \rangle = 0.5041 \pm 0.0042$) and HMS group ($\langle r \rangle = 0.6304 \pm 0.0246$). To show the difference among groups, we used gray lines with $\alpha = 1.47$ to guide the eyes. The corresponding group-aggregate branching parameters are $\sigma_{LMS} = 0.7237$ for the LMS group, $\sigma_{MMS} = 1.0123$ for the MMS group, and $\sigma_{HMS} = 1.2023$ for the HMS group. **d** Avalanche duration distributions for three groups in **c**. To show the difference among groups, we used gray lines with $\tau = 1.7$ to guide the eyes. **e** Scaling relationship for the three groups. The blue line and purple line correspond to γ and $\frac{\tau-1}{\alpha-1}$, respectively. In the inset, $\delta = \left|\gamma - \frac{\tau-1}{\alpha-1}\right|$ indicates the distance to the critical point. **f** Quantification of brain state against three levels of $\langle r \rangle$ using kappa κ, which was calculated in different numbers m of histogram bins.

As the above close check of hallmarks of criticality did not agree with each other well, we moved forward to investigate whether this mismatch could be a result of intersubject variability. We calculated both the MS and SE (see 2.2.1. Synchrony and variability in synchrony) using the $atlas_{96}$ signals for each of the 295 subjects and characterized the brain states of each subject with points in the MS vs. SE phase plane, as seen in the top panel of Fig. 2 **a**. We found that the value for MS from these subjects extended from 0.2 to 0.7, and the distribution of subjects was not even but exhibited a greater tendency to the low MS range (Fig. 2 **a**, bottom panel). This result suggested that even in the resting state, there is significant variability among the subjects' brain states. It is clearly seen that these state points formed an inverted-U trajectory in the phase plane. The SE exhibited a maximum at the moderate value of MS, which implied the existence of a state with dynamic richness between order and disorder. We found the inverted-U curves and the calculation of SE was robust against different parcellation (Fig. S2). We also performed a phase randomization method on the fMRI data and found that this inverted-U curve disappeared in the randomized surrogate datasets (size=500, identified by visual inspection; examples can be seen in Fig. S3). Therefore, we argued that this inverted-U curve reflected a special spatiotemporal structure of brain dynamics that did not exist in randomized data.

As expected, with the increasing of MS, the spatiotemporal activation pattern defined before exhibited transition from random states to ordered states (Fig. S4). We then calculated the branching parameter σ for each subject. We found that with increasing MS, the branching parameter increased from less than 1 to higher than 1, crossing 1 at a moderate value of MS (Fig. 2 **b**, and Fig S5 for different parcellation).

Furthermore, we selected three groups from the above subjects: the low mean synchronization group (LMS group; the 20 most left subjects in Fig. 2 **a** with an MS value of $\langle r \rangle = 0.2824 \pm 0.0219$), the moderate mean synchronization group (MMS group; the 20 subjects located near the peak of curve in Fig. 2 **a** with an MS value of $\langle r \rangle = 0.5041 \pm 0.0042$), and the high mean synchronization group (HMS group; the 20 most right subjects in Fig. 2 **a** with an MS value of $\langle r \rangle = 0.6304 \pm 0.0246$). For each group, we performed avalanche distribution analysis to identify which group was closest to the critical point (Fig. 2 **c-f**). After obtaining scaling

exponents α and τ for each group with a threshold of 1.4 SD (Fig. 2 **c** and **d**), the scaling relationship showed the best match for the MMS group (Fig. 2 **e**), and more detailed analysis results can be found in Fig. S6 in the Supplementary Information.

Previous study showed that the truncations of power-law fit have a dramatic impact on power-law exponents, particularly on the ratio $\frac{1-\tau}{1-\alpha}$, while γ barely changes (Destexhe and Touboul, 2020). To test the robustness of our results, we performed analysis in Fig 2 **c-e** with different fitting windows for avalanche size S ($S_{min} \in [1, 10]$, and $S_{max} \in [30, 60]$) and avalanche duration ($T_{min} \in [1, 5]$, and $T_{max} \in [9, 20]$). We found that the ratio of the number of fitting that met the critical criterion ($|(1-\tau)/(1-\alpha) - \gamma| < 0.1$ and Clauset's goodness-of-fit test $p > 0.1$) to all power-law-fit samples is highest for MMS group ($\varphi = 0.0346$ for LMS, $\varphi = 0.1103$ for MMS, $\varphi = 0.0266$ for MMS).

We also calculated κ, an often-used parameter that could distinguish the difference between data and the theoretically suggested power-law distribution (Fagerholm et al., 2015; Palva et al., 2013; Poil et al., 2012; Shew et al., 2009; Shew et al., 2011). As shown in Fig. 2 **f**, as the discrete bin number m increases, the κ values become stable. The stabilized κ is smaller than 1 for the LMS group but larger than 1 for the HMS and MMS groups. The κ value for MMS group was closest to 1. Therefore, the above results suggested that subjects' brains with moderate MS and maximal SE are poised closest to the critical point, supported by consistent hallmarks of criticality. On the other hand, the large dispersion of subjects among the phase space between asynchronous (subcritical) and synchronous (supercritical) states also provides an opportunity to investigate the phase transition in brains.

3.2. The complexity in the FC network is maximized by criticality

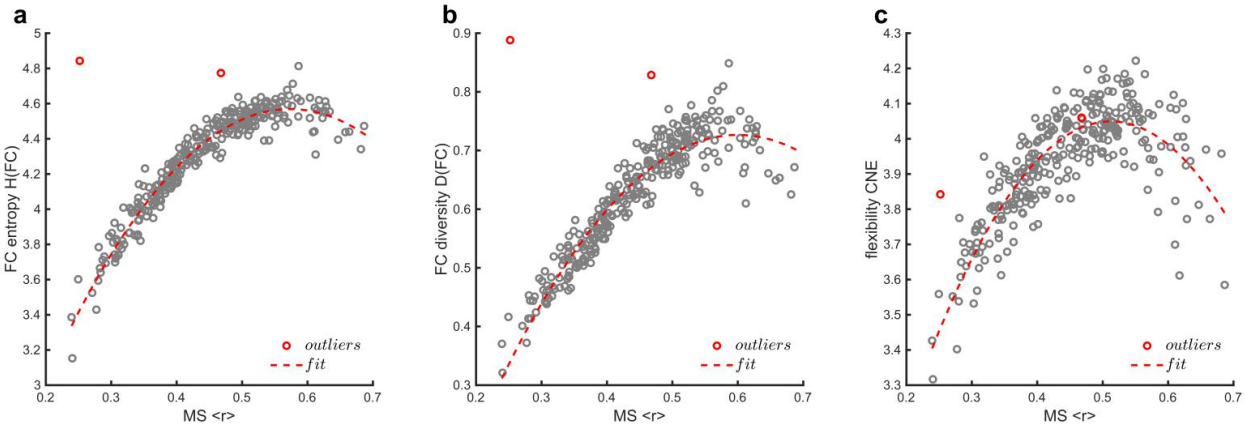

Figure 3 Dependence of complexity in the FC network on the MS of BOLD signals. a FC entropy $H(FC)$ as a function of MS $\langle r \rangle$. Dashed red line: quadratic fitting ($F = 2287.892$, p<0.001, adjusted $R^2 = 0.940$). **b** FC diversity $D(FC)$ as a function of MS $\langle r \rangle$. Dashed red line: quadratic fitting ($F = 1226.057$, p<0.001, adjusted $R^2 = 0.894$). **c** FC flexibility CNE as a function of MS $\langle r \rangle$. Dashed red line: quadratic fitting ($F = 366.851$, $p<0.001$, adjusted $R^2 = 0.715$). The red circles represent participants with outliers in the quadratic fittings in **a**, **b** and **c**.

Since the disorder-order phase transition could be observed, we investigated how this phase transition could impact the organization of FC networks. For convenience, we used MS to indicate this transition. We assessed how the variousness in FC strength changes as the brain undergoes a phase transition from the sub- to supercritical states. We used FC entropy and FC diversity as measures of variousness in FC strength in the brain networks. FC entropy is a direct measure of Shannon entropy from the probability distribution of FC strength obtained from the FC matrix, whereas FC diversity measures the similarity between the distribution of real FC matrix elements and uniform distribution. In previous studies, the former had been associated with healthy aging (Yao et al., 2013), and the latter is predicted to be maximized at the critical point by a computer model with Ginzburg-Landau equations (Wang et al., 2019). We found that both FC entropy (Fig. 3 **a**) and FC diversity (Fig. 3 **b**) peaked at the moderate value of MS; however, the peak position for these two measures was more rightward than that of SE.

The flexibility in dynamic FC reflects the extent of abundant connection patterns among regions and how frequent switching may occur between different patterns. In this work, we adopted the connection number entropy (CNE) as a measure of flexibility in FC networks. Our previous study showed that this measure was maximized at the critical point in a large-scale brain network model that combined DTI structural data and excitable cellular automaton (Song et al., 2019), and this measure could be reduced in the brains of patients with moyamoya disease (Lei et al., 2020). In this study, we found that the flexibility in FC was maximized with a moderate value of MS (Fig. 3 **c**). The maximization was robust in a wide range of THR_{FC} thresholds and sliding window lengths (Fig. S7). This result supported our previous conclusion (Lei et al., 2020; Song et al., 2019). Compared with FC entropy and FC diversity, the peak position for FC flexibility was nearer to the critical point.

FC entropy, diversity, and flexibility are often used in rfMRI studies to measure the complexity in the structure and dynamic reconfiguration of FC networks. Here, the study suggested that the complexity in FC networks is maximized by criticality.

3.3. The maximized structure-function coupling around the critical point

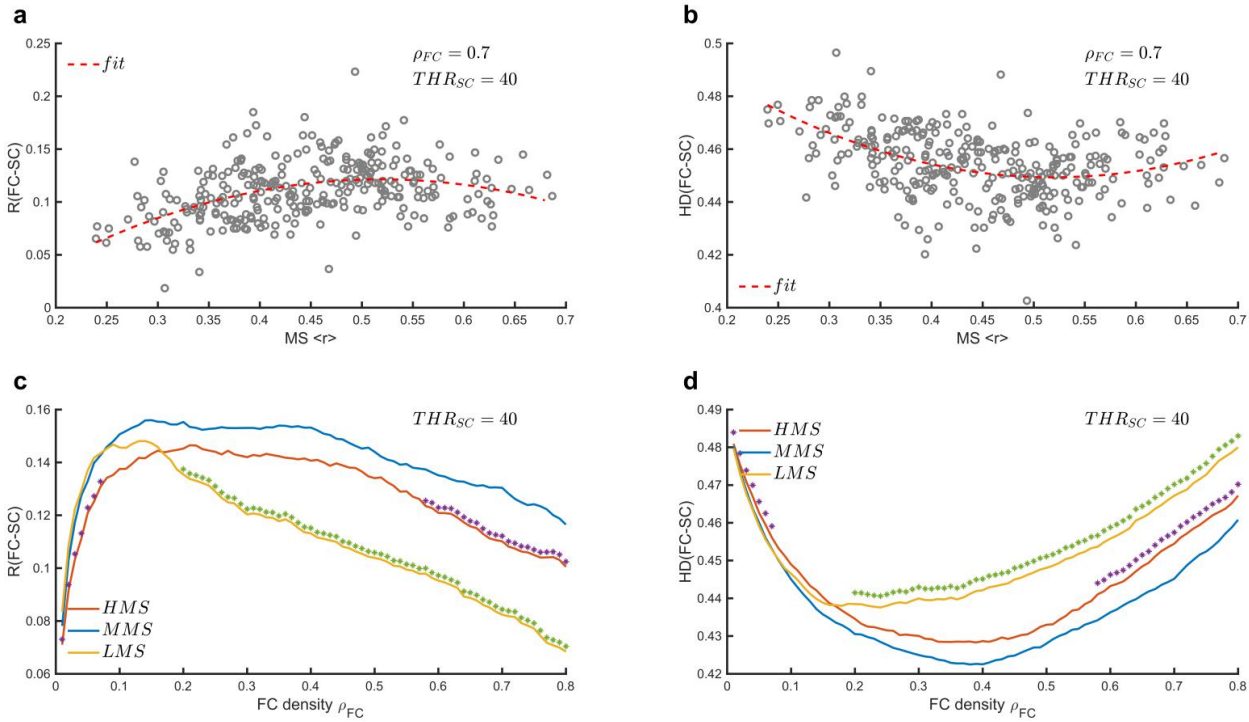

Figure 4 The dependence of structure-function coupling on the MS of brain network. a Pearson correlation between anatomical and functional networks as a function of MS $\langle r \rangle$. The link density in the FC network $\rho_{FC} = 0.7$ and threshold in the group-aggregated SC network THR_{SC}=40 (corresponding to $\rho_{SC} = 0.4836$) are shown in the figure. Dashed red line: quadratic fitting ($F = 36.997$, $p < 0.001$, adjusted $R^2 = 0.197$), which is better than linear fitting ($F = 39.346$, $p < 0.001$, adjusted $R^2 = 0.115$). **b** Hamming distance $HD(FC - SC)$ between anatomical and functional networks as a function of MS $\langle r \rangle$. Dashed red line: quadratic fitting (F=*36.997*, $p < 0.001$, adjusted R^2=0.197), which is better than linear fitting ($F = 39.346$, p<0.001, adjusted $R^2 = 0.115$). **c** The Pearson correlation between anatomical and functional networks as a function of FC density ρ_{FC} ($THR_{SC} = 40$ corresponding to $\rho_{SC} = 0.4826$) for the HMS, MMS, and LMS groups. **d** The Hamming distance between anatomical and functional networks as a function of FC density ρ_{FC} ($THR_{SC} = 40$ corresponding to $\rho_{SC} = 0.4826$) for the HMS, MMS, and LMS groups. In both **c** and **d**, green stars indicate significant differences

between the HMS and MMS groups (two-tails two-sample t-test, $p < 0.05$, uncorrected); purple stars indicate significant differences between the LMS and MMS groups (two-tails two-sample t-test, $p < 0.05$, uncorrected).

From the obtained FC matrix and SC matrix for each subject, we constructed the FC networks for each subject and a group-aggregated SC network (see 2.2.10 Similarity between functional and structural networks). We used THR_{FC} and THR_{SC} to control the link density in the FC networks and the group-aggregated SC network, respectively. We measured the similarity between the FC network and group-aggregated SC network with Pearson correlation and Hamming distance. Fig. 4 **a** and **b** demonstrate the dependence of similarity on the MS of each subject with a link density of 0.7 in the FC networks. The similarity between the FC and SC was maximal for subjects with moderate synchrony, as the Pearson correlation was maximized (Fig. 4 **a**), while the Hamming distance was minimized (Fig. 4 **b**) for these subjects. This maximization of similarity between the FC and SC could be observed in a wide range of link densities in the FC and SC networks. To further consolidate the above results, we measured the similarity between the FC and SC for the three groups (LMS MMS and HMS) defined above as a function of the FC network link density. Fig. 4 **c** and **d** show that as the FC network link density increased, the correlation coefficient between the FC and SC matrices first increased and then decreased, and consistently, the Hamming distance exhibited the opposite tendency. When the FC link density was large, the MMS group showed a significantly higher correlation and a lower Hamming distance between the FC and SC networks than the other two groups. Similarly, by varying THR_{SC}, we found that the maximized similarity in the FC and SC at the critical point was robust in the wide range of link densities in the SC network (Figs. S8, S9 and S10).

We noticed that for a large link density of the FC network, the dependence of similarity on link density monotonically decreased (Fig. 4 **c** and **d;** Fig. S8 **a** and **b**). Since lower link density conserved only stronger links in FC networks, we deduced that structural connections were mostly reflected in the strong functional connections. Meanwhile, the similarity also decreased as the threshold THR_{SC} in SC networks decreased (Fig. S9 **a** and **b**), suggesting that the

structural connections that were mostly reflected in the functional connection were those shared by most subjects because structural connections specified to individuals would be excluded with high THR_{SC}.

3.4. The dynamic phase transition in individual subjects' brains

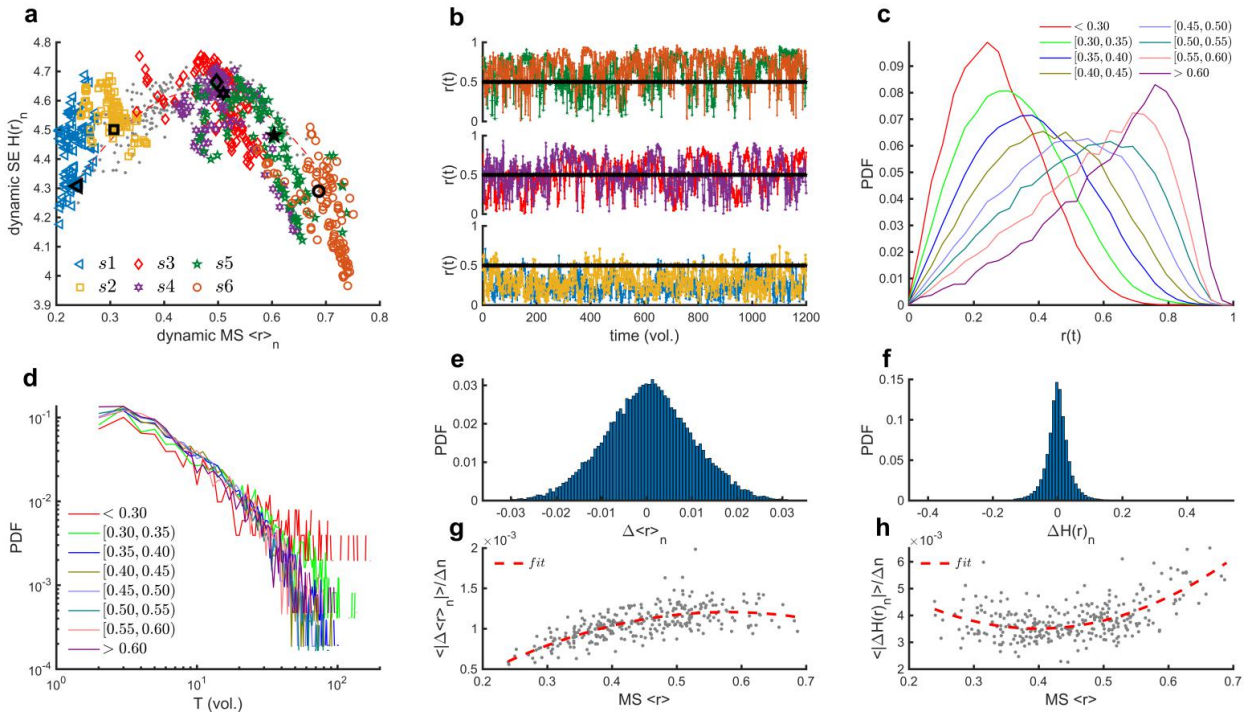

Figure 5 The dynamic phase transition in individual subjects' brains. a The dependence of dynamic SE $H(r)_n$ on dynamic MS $\langle r\rangle_n$ from six subjects selected randomly from the LMS, MMS, and HMS groups. The enlarged dark markers indicate the mean position for corresponding subjects (markers with the same shape). **b** The time-dependent changes in the Kuramoto order parameter $r(t)$ for six subjects as demonstrated in **a** (with the same color). **c** The normalized frequency count of $r(t)$ for different levels of $\langle r\rangle$, indicated by lines with different colors. **d** The dwell time (the time interval between two successive critical point crossing events) distribution for different levels of $\langle r\rangle$. **e** and **f** The distribution of vertical and horizontal moving distances of phase points in one step of the sliding window. **g** and **h** The vertical and horizontal velocities of state points of each subject as a function of their MS $\langle r\rangle$. The vertical and horizontal velocities were calculated by $\frac{\langle|\Delta\langle r\rangle_n|\rangle}{\Delta n}$ and $\frac{\langle|\Delta\langle r\rangle_n|\rangle}{\Delta n}$, where the symbol

$|\cdot|$ indicates the absolute value, and $\langle\cdot\rangle$ was the average across all the windows. Δn is the step used to slide the windows. Here, Δn=10 time points (volumes). Red dashed lines in **g** and **h**: quadratic fitting ($F = 139.316$, $p < 0.001$, adjusted $R^2 = 0.485$ in **g**; $F = 81.181$, $p < 0.001$, adjusted $R^2 = 0.353$ in **h**). Both quadratic fittings were better than linear fitting (adjusted $R^2 = 0.407$ in **g** and adjusted $R^2 = 0.173$ in **h**).

The observed individual brain states dispersed around the critical point provided an opportunity to investigate the dynamic phase transition in individual brains. To this end, for the LMS, MMS, and HMS groups defined above, we randomly selected two subjects from each group. We calculated the dynamical MS $\langle r\rangle_n$ and SE $H(r)_n$ for these six subjects with the sliding window approach (Fig. 5 **a**, s1-s6) from their Kuramoto order parameters $r(t)$ (Fig. 5 **b**). We observed a time-dependent change in individuals' brain states in the state space following the inverted-U trajectory, as shown in the top panel of Fig. 2 **a**. In the time period limited by scan duration, we observed that subjects who were farther away from the critical point tended to stay in the regime decided by MS, and events of crossing the critical point (black lines at $r(t) = 0.5$) to the other regime seldom occurred (s1, s2, s5, and s6 in Fig. 5 **a**, or Fig. 5 **b**, top and bottom panel). Subjects who were nearer the critical point were more likely to cross the critical point, which resembled the phase transitions in physics systems (s3 and s4 in Fig. 5 **a**, or Fig. 5 **b**, middle panel).

To validate the above observation at the population level, we divided the 295 subjects at hand into eight groups with different levels of synchrony and calculated the corresponding probability distribution of the Kuramoto order parameter $r(t)$. It is seen clearly from Fig. 5 **c** that as the synchrony level decreases, the distribution of the Kuramoto order parameter becomes narrow and less tilted. Meanwhile, we found that the dwell time, which referred to the time interval between two successive critical point crossing events, exhibited heavier tails in its distribution for low synchrony groups (Fig. 5 **d**). These results implied the higher inertness in the subcritical regime than others, and brains were more likely to stay in this regime with longer dwell times.

Next, we calculated the distribution of vertical and horizontal moving distances $\Delta\langle r\rangle_n$ and $\Delta H(r)_n$ in state space in a fixed time interval Δn (the time points or volumes of one step of the sliding window) for all subjects. We found that the distributions of vertical and horizontal moving distances were both symmetrical with a mean of zero (Fig. 5 **e** and **f**), suggesting that the inverted-U trajectory in the state space was stable and unlikely to change its shape as time progressed. Furthermore, the position ($\langle r\rangle$) dependent velocity distribution is maximal for horizontal velocity ($\frac{\langle|\Delta\langle r\rangle_n|\rangle}{\Delta n}$) and minimal for vertical velocity ($\frac{\langle|\Delta\langle r\rangle_n|\rangle}{\Delta n}$) near the critical point. The maximal horizontal velocity around the critical point implied that at this point, the systems were most sensitive to the perturbations due to internal fluctuations or external modulations. Meanwhile, the lower vertical and horizontal velocities in the subcritical regime compared to the supercritical regime also reflected the high inertness in the subcritical regime.

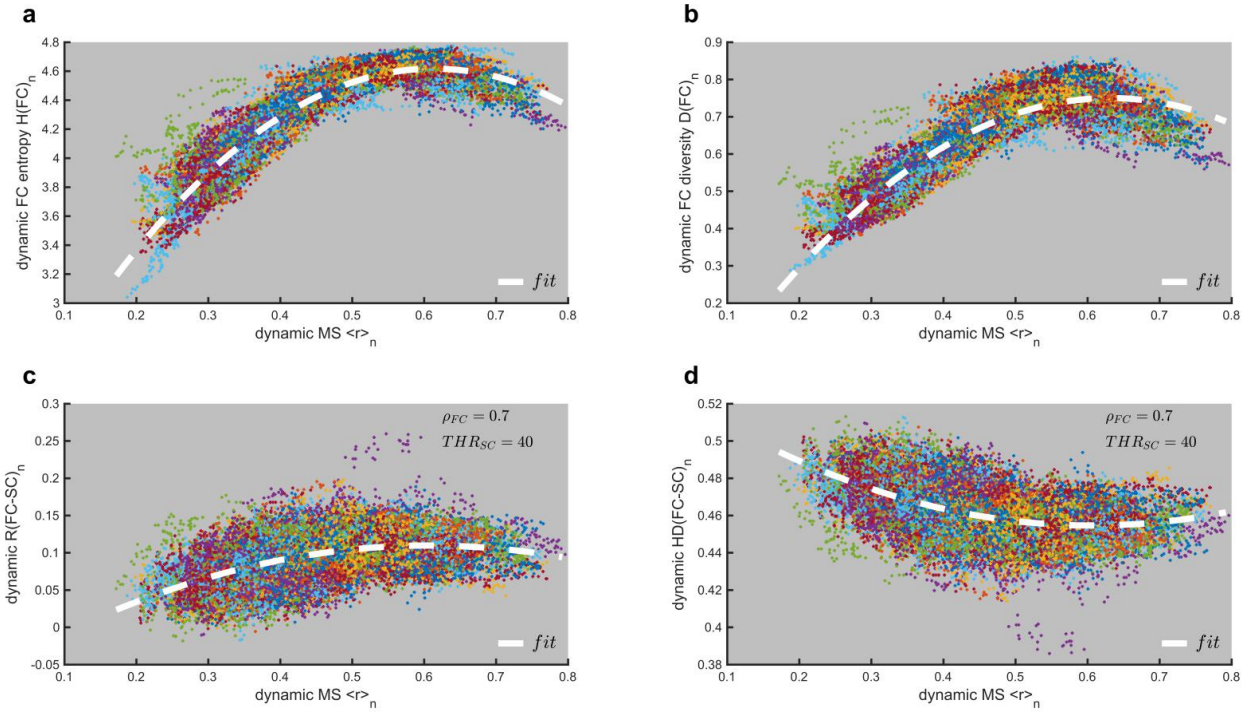

Figure 6 Dynamic modulations of FC complexity and structure-function coupling during the phase transition of brains. a The dependence of dynamic FC entropy as a function of instantaneous MS; thick dashed white line: quadratic fitting ($F = 106350.82$, $p < 0.001$, adjusted $R^2 = 0.877$). **b** The dependence of dynamic FC diversity as a function of instantaneous MS. Thick dashed white line: quadratic fitting ($F = 80261.492$, $p < 0.001$,

adjusted $R^2 = 0.843$). **c** The dependence of dynamic FC-SC correlation as a function of instantaneous MS; thick dashed white line: quadratic fitting ($F = 5519.072$, $p < 0.001$, adjusted $R^2 = 0.270$), which is better than linear fitting (adjusted $R^2 = 0.225$). **d** The dependence of dynamic FC-SC Hamming distance as a function of instantaneous MS; thick dashed white line: quadratic fitting ($F = 5519.072$, $p < 0.001$, adjusted $R^2 = 0.270$), which is better than linear fitting (adjusted $R^2 = 0.225$). In **a-d**, each dot represents a calculation from one window. The dots with the same color represent the calculation for one subject. However, due to the limited number of colors used, different subjects may share the same color. In **c-d**, a link density of 0.7 was used to obtained the binary FC network, and a threshold of 40 was used to obtained the group-aggregated structural network.

It was of interest to determine whether the maximization of FC complexity, as well as function-structure coupling, around the critical point could be realized dynamically when the individual brains endured phase transition. To this end, we obtained the time-dependent FC matrices with the sliding window method and calculated FC entropy (Fig. 6 **a**), FC diversity (Fig. 6 **b**), and two measures for similarity between FC and SC (Fig. 6 **c** and **d**) as a function of instantaneous MS in each time window. The time-dependent complexity and similarity measures followed almost the exact trajectories as those in the static measurements shown in Fig. 3 **a** and **b**, as well as Fig. 4 **a** and **b**. This result implied that FC complexity and similarity between FC and SC were indeed modulated by phase transition in brains, and their maximization could be realized dynamically by positioning the system around the critical point.

3.5. High fluid intelligence and working memory capacity were associated with critical dynamics

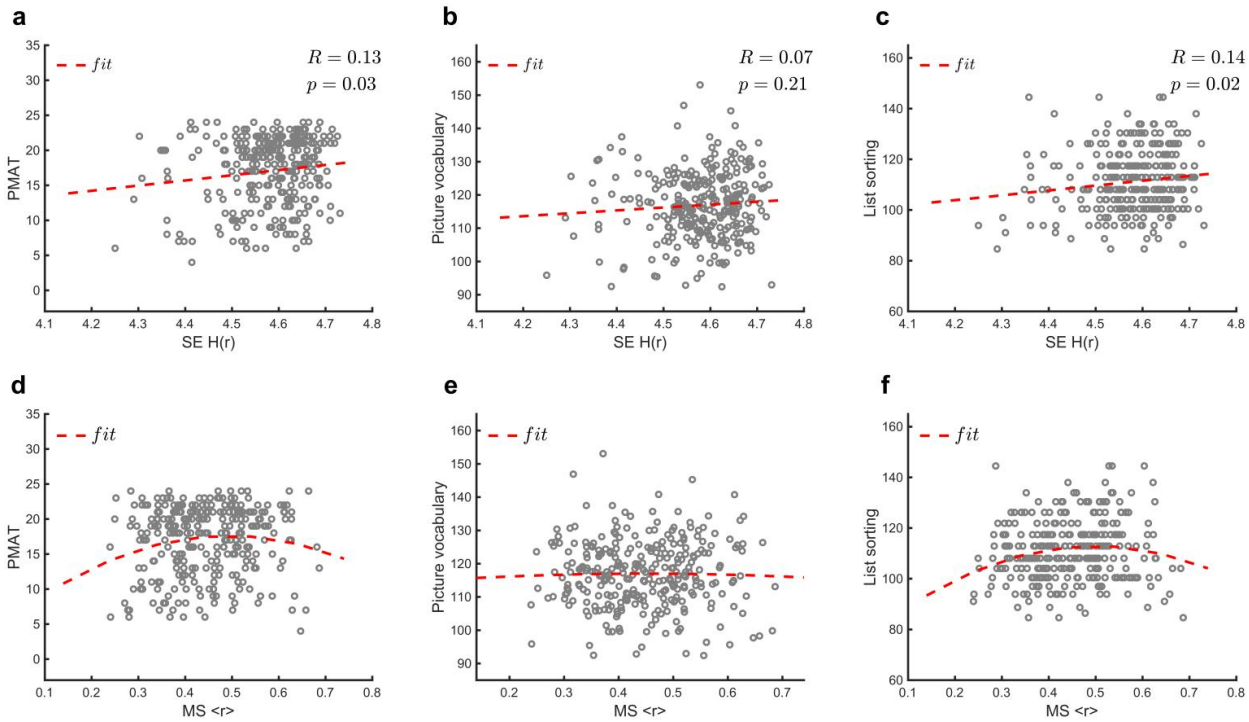

Figure 7 Correlations between cognitive performance scores and SE, as well as MS. **a-c** Correlation between SE and PMAT scores, picture vocabulary test scores, as well as the list sorting working memory test scores. Dashed red lines in **a-c**: linear fitting. **d** Scatterplot of the PMAT scores against the MS. The red dashed line represents the significant quadratic fit of the data ($F = 3.109$, $p = 0.046$, adjusted $R^2 = 0.014$), which is better than the linear fitting (adjusted $R^2 = 0.004$). **e** Scatterplot of the picture vocabulary test scores against the MS. Both the linear and quadratic regressions are not significant (linear: $p = 0.983$; quadratic: $p = 0.971$). **f** Scatterplot of the list sorting working memory test scores against the MS. The red dashed line represents the significant quadratic fit of the data ($F = 4.401$, $p = 0.013$, adjusted $R^2 = 0.023$), which is better than linear fitting (adjusted $R^2 = 0.009$).

The results above support the hypothesis that large-scale brain networks lie in the vicinity of a critical point which associated with moderate MS and maximal SE. Another key prediction from

the critical brain hypothesis is that brains that are closer to criticality should be better in cognitive performance. Here, to address this prediction, we assessed linear relationships between SE and intelligence scores of the available subjects. We found that SE values were significantly correlated with fluid intelligence scores (PMAT; Fig. 7 **a**) but not with crystallized intelligence scores (picture vocabulary; Fig. 7 **b**). Meanwhile, we found that working memory scores, which were assessed using the Listing Sorting Working Memory test from the NIH Toolbox, were significantly correlated with SE (List sorting; Fig. 7 **c**). We also noted here that these scores were significantly correlated with many other measures that were found to be maximized at the criticality, namely, FC entropy, FC diversity, and FC flexibility (Fig. S11 in Supplementary Materials). Meanwhile, there were significant quadratic functions between MS and fluid intelligence and working memory scores but not crystallized intelligence scores (Fig. 7 **d-f**). And the Age-adjusted cognitive scores present similar results to above (figures are not shown). Therefore, these results support the hypothesis that brains that are closer to criticality are associated with higher fluid intelligence and working memory scores.

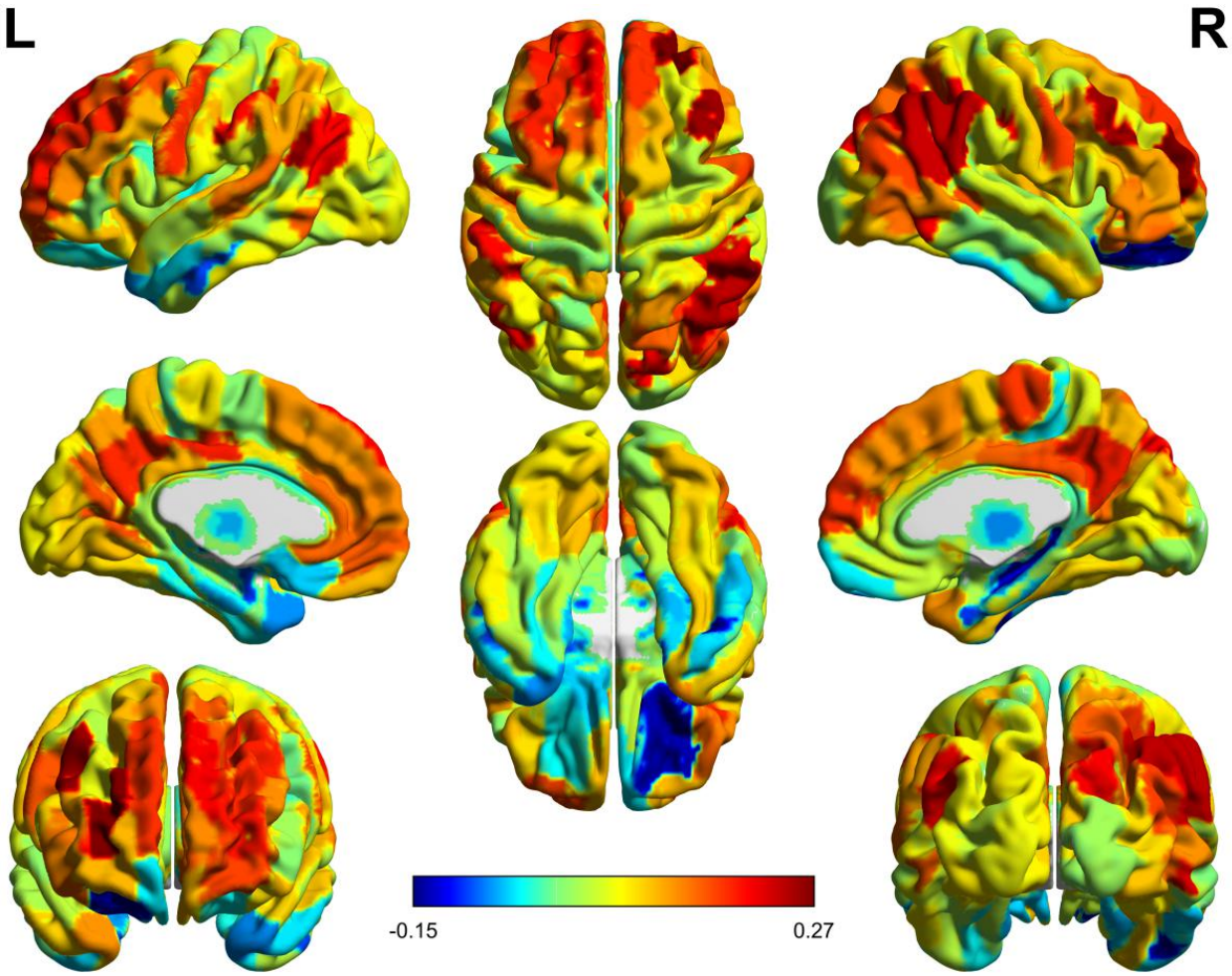

Figure 8 The brain map for correlations between regional SE and fluid intelligence. The color bar indicated the Pearson correlation value (i.e. R) between regional SE and PMAT. The cortical and subcortical regions were defined by the Human Brainnetome Atlas. Data was visualized using BrainNet Viewer (Xia et al., 2013).

Table 1 The brain regions exhibited significant correlation between SE and fluid intelligence.

Lobe	Gyrus	Left/Right	Brodmann area	MNI coordinate	R	FDR
Frontal Lobe	Superior Frontal Gyrus (SFG)	SFG_L_7_3	8, 9, 10	[-11, 49, 40]	0.2058	0.0118
		SFG_R_7_3	8, 9, 10	[13, 48, 40]	0.1762	0.0310
		SFG_R_7_7	10	[8, 58, 13]	0.1756	0.0310
	Middle Frontal Gyrus (MFG)	MFG_L_7_1	9, 46	[-27, 43, 31]	0.1821	0.0265
		MFG_L_7_3	10, 11, 46	[-28, 56, 12]	0.1922	0.0201
		MFG_R_7_3	9, 10, 46	[28, 55, 17]	0.2699	0.0007
		MFG_L_7_5	8, 9, 44, 46	[-33, 23, 45]	0.1859	0.0237
		MFG_R_7_5	9, 44, 45, 46	[42, 27, 39]	0.2537	0.0015
		MFG_L_7_7	10, 11, 47	[-26, 60, -6]	0.1673	0.0398
	Inferior Frontal Gyrus (IFG)	IFG_R_6_5	45, 47	[42, 22, 3]	0.1819	0.0265
	Precentral Gyrus (PrG)	PrG_L_6_1	4, 6	[-49, -8, 39]	0.1793	0.0277
		PrG_R_6_1	4, 6	[55, -2, 33]	0.1711	0.0351
	Paracentral Lobule (PCL)	PCL_R_2_2	4, 6	[5, -21, 61]	0.1730	0.0329
Temporal Lobe	Inferior Temporal Gyrus (ITG)	ITG_R_7_5	20, 21, 37	[54, -57, -8]	0.2050	0.0118
Parietal Lobe	Superior Parietal Lobule (SPL)	SPL_R_5_5	7, 40	[31, -54, 53]	0.1731	0.0329
	Angular Gyrus (AG)	IPL_R_6_1	39	[45, -71, 20]	0.1681	0.0397
		IPL_R_6_2	7, 39	[39, -65, 44]	0.2374	0.0027
		IPL_L_6_5	39	[-47, -65, 26]	0.2016	0.0133
		IPL_R_6_5	39	[53, -54, 25]	0.2295	0.0038
	Supramarginal Gyrus (SG)	IPL_L_6_3	2, 3, 40	[-51, -33, 42]	0.1991	0.0142
		IPL_R_6_3	2, 3, 40	[47, -35, 45]	0.2073	0.0118
		IPL_R_6_4	2, 40	[57, -44, 38]	0.2369	0.0027
	Precuneus (Pcun)	Pcun_L_4_4	7	[-6, -55, 34]	0.1808	0.0267
		Pcun_R_4_4	7	[6, -54, 35]	0.1871	0.0237
Limbic Lobe	Cingulate Gyrus (CG)	CG_L_7_6	23	[-7, -23, 41]	0.1868	0.0237
Occipital Lobe	Superior Occipital Gyrus (sOcG)	sOcG_R_2_1	18, 19	[16, -85, 34]	0.2061	0.0118

Abbreviation: IPL, Inferior Parietal Lobule.

Since a wide variety of experiments have demonstrated that fluid intelligence is associated with a distributed network of regions in the Parieto-Frontal Integration Theory (P-FIT), including frontal areas (Brodmann areas (BAs) 6, 9, 10, 45-47), parietal areas (BA 7, 39, 40), visual cortex (BAs 18, 19), fusiform gyrus (BA 37), Wernicke's area (BA 22) and dorsal anterior cingulate cortex (BA 32) (Jung and Haier, 2007; Nikolaidis et al., 2017), we decided to find more relationships between these regions with critical dynamics indicated by maximized SE. To obtain the relevant regions in a fine-grained division of the brain, here we used the Human Brainnetome Atlas, which contains 210 cortical and 36 subcortical subregions (Fan et al., 2016). We extracted from each brain region the voxel-level BOLD signals and calculated the regional SE for these 246 regions. We found that regions whose SE exhibited significant ($p < 0.05$, FDR corrected) positive correlations with PMAT scores were located in the frontal areas (i.e. bilateral SFG, MFG, PrG, right IFG and PCL), parietal areas (i.e. bilateral AG, SMG, Pcun, right SPL), right inferior

temporal gyrus (ITG), superior occipital gyrus (sOcG) and left Cingulate gyrus (CG) (details in Fig 8 and Table 1).

4. Discussion

In this study, we introduced a novel yet simple method to uncover the criticality and phase transition of brain dynamics through resting-state fMRI data analysis. With this method, subjects were mapped into a trajectory where the critical point, as well as sub- and supercritical regimes, divided by the critical point, could be identified. These results support the critical brain hypothesis - with avalanche criticality - under a second-order phase transition. We observed that the complexity in brain FC was maximized around the critical point, as was the structure-function coupling. Therefore, our findings validated two predictions of criticality in large-scale networks. We proceeded to observe a dynamic phase transition in individual subjects, and found that their brains tended to stay subcritical, as indicated by a longer dwell time in this parameter region. Finally, we found that high fluid intelligence and working memory capacity were associated with critical dynamics rather than noncritical dynamics, not only globally but also regionally, suggesting the functional advantages of critical dynamics in resting-state brains.

Functional segregation and functional integration is a central organizing principle of the cerebral cortex. It has been argued that FC complexity characterizes the interplay of functional segregation and functional integration (Sporns, 2013). A comparison between simulated and empirically obtained resting-state FC indicates that the human brain at rest, lies in a dynamic state that reflects the largest complexity its anatomical connectome can host (Tononi et al., 1994). Recently, many studies have tried to link complexity with cognitive performance, human intelligence, and even consciousness, either measured by Φ (big phi) in integrated information theory or discriminated between levels of sedation (Ahmadlou et al., 2014; Duncan et al., 2017; Saxe et al., 2018; Tononi et al., 1998). Meanwhile, there is a growing awareness that complexity is strongly related to criticality. A recent study showed that criticality maximized complexity in dissociated hippocampal cultures produced from rats (Timme et al., 2016). Here, in this study, we measured FC complexity from different perspectives, either on its strength diversity or on its

730 dynamic flexibility (Fig. 3 **a-c**, Fig. 6 **a** and **b**). With the observation of the phase transition
731 trajectory, we demonstrated that these measures of FC complexity were maximized around the
732 critical point. Therefore, the formulation that criticality maximizes complexity was supported in
733 our work empirically with fMRI data at the whole-brain network level.

734 It has been shown that human brains possess a stable set of functionally coupled networks that
735 echo many known features of anatomical organization (Krienen et al., 2014). Several
736 computational modeling studies have demonstrated that critical dynamics could best explore the
737 repertoire provided by the structural connectome (Deco and Jirsa, 2012; Tagliazucchi et al.,
738 2016). Recent studies also suggested the capacity of repertoire provided by the structural
739 connectome could be extend by the hierarchical modular structural organization (Wang et al.,
740 2019). Therefore, structure-function coupling was believed to be at its maximal when the
741 system is at criticality (Wang et al., 2019), and it could be disrupted by losing criticality (Cocchi
742 et al., 2014), or disruption of hierarchical organization of structural networks. Previous studies in
743 anesthetized human brains have found structure-function decoupling accompanied by
744 unidirectional departure from a critical point (Tagliazucchi et al., 2016). It is possible that
745 functional connectivity flexibility could be used as a measure of the extent that functional
746 connectivity explores the repertoire provided by structural connectome, and the highest
747 functional connectivity flexibility occurs when the system is at criticality (Song et al., 2019) (Fig.
748 3 **c**). Our work demonstrated the maximal exploration of structural connections at the critical
749 point occur in resting state brains (Fig. 4). However, since we used a group aggregated structural
750 connection networks, we did not investigate how organization of structural connections could
751 impact on the capacity of network repertoire. This issue will be investigated in the future.

752 Interestingly, although the brain hovers around the critical point, the brain prefers to stay in the
753 subcritical region, as the subject distribution was skewed toward a disordered state, and the dwell
754 time in the subcritical state was longer (Fig. 5). Previous analysis of in vivo data has argued that
755 the mammalian brain self-organizes to a slightly subcritical regime (Priesemann et al., 2014). It
756 was suggested that operating in a slightly subcritical regime may prevent the brain from tipping
757 over to supercriticality, which has been linked to epilepsy. Meanwhile, with a slightly subcritical

regime deviates only little from criticality, the computational capabilities may still be close to optimal. However, our results showed that the resting state brains could actually stay in the supercritical regimes. So, the preference of brains for subcritical regime may not because of prevention of too ordered states. In another study, by relating the EEG-domain cascades to spatial BOLD patterns in simultaneously recorded fMRI data, the researchers found that while resting-state cascades were associated with an approximate power-law form, the task state was associated with subcritical dynamics (Fagerholm et al., 2015). They argued that while a high dynamic range and a large repertoire of brain states may be advantageous for the resting state with near-critical dynamics, a lower dynamic range may reduce elements of interference affecting task performance in a focused cognitive task with subcritical dynamics (Fagerholm et al., 2015). Therefore, there remains a possibility that the resting state is not "pure resting state", but mixed with some occasional "task state" for some subjects. However, further delicately designed experimental studies are required to test this conjecture. It remains to uncover the relationship between cognitive states and neural dynamics that lies on a spectrum. The method proposed in this study may be useful in future studies of this topic.

Recently, Ezaki et al. used the Ising model to map BOLD signals on a two-dimensional phase space and found that human fMRI data were in the paramagnetic phase and were close to the boundary with the spin-glass phase but not to the boundary with the ferromagnetic phase (Ezaki et al., 2020). Since the spin-glass phase usually yields chaotic dynamics whereas the ferromagnetic phase is nonchaotic, their results suggested that the brain is around the "edge of chaos criticality" instead of "avalanche criticality". However, our findings support that avalanche criticality occur in large-scale brain networks. Therefore, it is interesting to investigate whether both kinds of criticality could co-occur in large-scale brain networks (Kanders et al., 2017). Ezaki et al. also found that criticality of brain dynamics was associated with human fluid intelligence, though they used performance IQ to reflect fluid intelligence, which refers to active or effortful problem solving and maintenance of information. In our work, we assessed the correlation between fluid intelligence and the critical dynamics indicated by synchronization entropy for brain regions, and found regions showed significant positive correlations were

located in parietal-frontal network (Fig. 8 and Table 1). These regions were most frequently reported in studies of intelligence and its biological basis, including structural neuroimaging studies using voxel-based morphometry, magnetic resonance spectroscopy, and DTI, as well as functional imaging studies using positron emission tomography (PET) or fMRI (Jung and Haier, 2007). Also, in the Parieto-Frontal Integration Theory of intelligence, these regions are considered as the most crucial nodes of the brain network underlying human intelligence (Jung and Haier, 2007; Nikolaidis et al., 2017).

Our study suggested that not only fluid intelligence, but also working memory capacity was associated with critical dynamics. This is possibly because working memory may share the same capacity constraint through similar neural networks with fluid intelligence (Halford et al., 2007; Jaeggi et al., 2008; Kane and Engle, 2002). In our study, the critical dynamics in the frontal and parietal network also exhibited high correlation with working memory capacity (Fig. S12 and Table S1). Furthermore, it has been well established that working memory is strongly modulated by dopamine, and too strong or too weak dopamine D1 activation is detrimental for working memory, with the optimal performance achieved at an intermediate level (Cools and D'Esposito, 2011; Vijayraghavan et al., 2007; Zahrt et al., 1997). This inverted-U dose-response has been observed in mice (Lidow et al., 2003), rats (Zahrt et al., 1997), monkeys (Cai and Arnsten, 1997) and humans (Gibbs and D'Esposito, 2005). Recent studies on neural network models have shown that the optimal performance of working memory co-occurs with critical dynamics at the network level and the excitation-inhibition balance at the level of individual neurons and is modulated by dopamine at the synaptic level through a series of U or inverted-U profiles (Hu et al., 2019). Here in this study, we demonstrated that the optimal performance of working memory and criticality co-occurs at the system level.

However, our study had several limitations. Firstly, the surrogate data test used in this study ruled out the possibility that the results we obtained can be explained by autocorrelations in the data. However, the long-range spatial correlation of criticality cannot allow one to test the results by ruling out of the effects of correlation across the time series. Secondly, though we used the denoising fMRI data from HCP with standard data pre-processing procedure, it is still interesting

to investigate the pre-processing procedure affects the results. Thirdly, in the avalanche analysis, the activation events defined in this study was slightly different from definition used by others, such as threshold-crossing events (Tagliazucchi et al., 2012) or threshold-above events (Bocaccio et al., 2019; Wang et al., 2019). We compared these different methods and found all these methods could generate scale free avalanche activities, but unlike our method, the other two methods failed to generate critical branching process in consistent with theory (See Section II in Supplementary Materials). Therefore, it is interesting to investigate the correlations between neural activities and events detected by different detection methods from BOLD signals.

5. Conclusions

In conclusion, we proposed a simple approach to map individuals' brain dynamics from resting-state fMRI scans on the phase transition trajectory and identify subjects who are close to the critical point. With this approach, we validated two predictions of critical brain hypothesis on large-scale brain networks, i.e., maximized FC complexity and maximized structure-function coupling around the critical point. We also observed the tendency of brain to stay in subcritical regime. Finally, we found that the critical dynamics in large-scale brain networks were associated with high scores in fluid intelligence and working memory, implying the vital role of large-scale critical dynamics in cognitive performance. We also identified key brain regions whose critical dynamics was highly correlated with human intelligence. Our findings support the critical brain hypothesis that neural computation is optimized by critical brain dynamics, as characterized by scale-free avalanche activity, and could provide a solution for improving the effects of future interventions targeting aspects of cognitive decline (Reinhart and Nguyen, 2019), possibly by control the criticality through non-invasive stimulation (Chialvo et al., 2020).

Data and code availability

The rfMRI data, DTI data and cognitive data are available from the Human Connectome Project at humanconnectome.org, WU-Minn Consortium. The WU-Minn HCP Consortium obtained full informed consent from all participants, and research procedures and ethical guidelines were followed in accordance with the Washington University Institutional Review Boards (IRB #201204036; Title: 'Mapping the Human Connectome: Structure, Function, and Heritability'). MATLAB (https://www.mathworks.com/) and SPSS (https://www.ibm.com/analytics/spss-statistics-software) were used to conduct the experiment's reported in this study.

Declaration of Competing interest

The authors declare no competing interests.

CRediT authorship contribution statement

Longzhou Xu: Methodology, Software, Validation, Formal analysis, Investigation, Data Curation, Writing – Original Draft, Writing – Review & Editing, Visualization.

Lianchun Yu: Conceptualization, Methodology, Data Curation, Validation, Resources, Writing – Original Draft, Writing – Review & Editing, Supervision, Project administration, Funding acquisition.

Jianfeng Feng: Conceptualization, Writing – Review & Editing, Supervision, Funding acquisition.

Role of the Funding Source

This study was funded by the National Natural Science Foundation of China (Grants No. 11105062) and the Fundamental Research Funds for the Central Universities (Grant No. lzujbky-2015-119). J. F. is supported by the 111 Project (Grant No. B18015), the National Key R&D Program of China (No.2018YFC1312904; No.2019YFA0709502), the Shanghai Municipal

Science and Technology Major Project (Grant No. 2018SHZDZX01), ZJLab, and Shanghai Center for Brain Science and Brain-Inspired Technology.

References

Ahmadlou, M., Adeli, A., Bajo, R., Adeli, H., 2014. Complexity of functional connectivity networks in mild cognitive impairment subjects during a working memory task. Clinical Neurophysiology 125, 694-702.

Anokhin, A.P., Birbaumer, N., Lutzenberger, W., Nikolaev, A., Vogel, F., 1996. Age increases brain complexity. Electroencephalography and Clinical Neurophysiology 99, 63-68.

Barch, D.M., Burgess, G.C., Harms, M.P., Petersen, S.E., Schlaggar, B.L., Corbetta, M., Glasser, M.F., Curtiss, S., Dixit, S., Feldt, C., Nolan, D., Bryant, E., Hartley, T., Footer, O., Bjork, J.M., Poldrack, R., Smith, S., Johansen-Berg, H., Snyder, A.Z., Van Essen, D.C., Consortium, W.U.-M.H., 2013. Function in the human connectome: task-fMRI and individual differences in behavior. Neuroimage 80, 169-189.

Beggs, J., Timme, N., 2012. Being Critical of Criticality in the Brain. Frontiers in Physiology 3, 163.

Beggs, J.M., Plenz, D., 2003. Neuronal avalanches in neocortical circuits. The Journal of neuroscience : the official journal of the Society for Neuroscience 23, 11167-11177.

Bilker, W.B., Hansen, J.A., Brensinger, C.M., Richard, J., Gur, R.E., Gur, R.C., 2012. Development of Abbreviated Nine-Item Forms of the Raven's Standard Progressive Matrices Test. Assessment 19, 354-369.

Bocaccio, H., Pallavicini, C., Castro, M.N., Sánchez, S.M., De Pino, G., Laufs, H., Villarreal, M.F., Tagliazucchi, E., 2019. The avalanche-like behaviour of large-scale haemodynamic activity from wakefulness to deep sleep. Journal of The Royal Society Interface 16, 20190262.

Cai, J.X., Arnsten, A.F.T., 1997. Dose-Dependent Effects of the Dopamine D1 Receptor Agonists A77636 or SKF81297 On Spatial Working Memory in Aged Monkeys. Journal of Pharmacology and Experimental Therapeutics 283, 183.

Chialvo, D.R., Cannas, S.A., Grigera, T.S., Martin, D.A., Plenz, D., 2020. Controlling a complex system near its critical point via temporal correlations. Scientific Reports 10, 12145.

Clauset, A., Shalizi, C.R., Newman, M.E.J., 2009. Power-Law Distributions in Empirical Data. SIAM Review 51, 661-703.

Cocchi, L., Gollo, L.L., Zalesky, A., Breakspear, M., 2017. Criticality in the brain: A synthesis of neurobiology, models and cognition. Progress in Neurobiology 158, 132-152.

Cocchi, L., Harding, I.H., Lord, A., Pantelis, C., Yucel, M., Zalesky, A., 2014. Disruption of structure–function coupling in the schizophrenia connectome. NeuroImage: Clinical 4, 779-787.

Cools, R., D'Esposito, M., 2011. Inverted-U Shaped Dopamine Actions on Human Working Memory and Cognitive Control. Biological Psychiatry 69, e113-e125.

Deco, G., Jirsa, V.K., 2012. Ongoing Cortical Activity at Rest: Criticality, Multistability, and Ghost Attractors. The Journal of Neuroscience 32, 3366.

Deco, G., Jirsa, V.K., McIntosh, A.R., 2011. Emerging concepts for the dynamical organization of resting-state activity in the brain. Nature Reviews Neuroscience 12, 43-56.

Deluca, A., Corral, Á., 2013. Fitting and goodness-of-fit test of non-truncated and truncated power-law distributions. Acta Geophysica 61, 1351-1394.

Destexhe, A., Touboul, J., 2020. Comment on "Criticality Between Cortical States". arXiv: Neurons and Cognition.
Duncan, J., Chylinski, D., Mitchell, D.J., Bhandari, A., 2017. Complexity and compositionality in fluid intelligence. Proceedings of the National Academy of Sciences 114, 5295.
Ezaki, T., Fonseca dos Reis, E., Watanabe, T., Sakaki, M., Masuda, N., 2020. Closer to critical resting-state neural dynamics in individuals with higher fluid intelligence. Communications Biology 3, 52.
Fagerholm, E.D., Lorenz, R., Scott, G., Dinov, M., Hellyer, P.J., Mirzaei, N., Leeson, C., Carmichael, D.W., Sharp, D.J., Shew, W.L., Leech, R., 2015. Cascades and cognitive state: focused attention incurs subcritical dynamics. The Journal of neuroscience : the official journal of the Society for Neuroscience 35, 4626-4634.
Fan, L., Li, H., Zhuo, J., Zhang, Y., Wang, J., Chen, L., Yang, Z., Chu, C., Xie, S., Laird, A.R., Fox, P.T., Eickhoff, S.B., Yu, C., Jiang, T., 2016. The Human Brainnetome Atlas: A New Brain Atlas Based on Connectional Architecture. Cerebral Cortex 26, 3508-3526.
Fontenele, A.J., de Vasconcelos, N.A.P., Feliciano, T., Aguiar, L.A.A., Soares-Cunha, C., Coimbra, B., Dalla Porta, L., Ribeiro, S., Rodrigues, A.J., Sousa, N., Carelli, P.V., Copelli, M., 2019. Criticality between Cortical States. Phys Rev Lett 122, 208101.
Friedman, N., Ito, S., Brinkman, B.A.W., Shimono, M., DeVille, R.E.L., Dahmen, K.A., Beggs, J.M., Butler, T.C., 2012. Universal Critical Dynamics in High Resolution Neuronal Avalanche Data. Physical Review Letters 108, 208102.
Gal, A., Marom, S., 2013. Self-organized criticality in single-neuron excitability. Physical Review E 88, 062717.
Gibbs, S.E.B., D'Esposito, M., 2005. A functional MRI study of the effects of bromocriptine, a dopamine receptor agonist, on component processes of working memory. Psychopharmacology 180, 1-10.
Gireesh, E.D., Plenz, D., 2008. Neuronal avalanches organize as nested theta- and beta/gamma-oscillations during development of cortical layer 2/3. Proceedings of the National Academy of Sciences 105, 7576.
Glasser, M.F., Smith, S.M., Marcus, D.S., Andersson, J.L.R., Auerbach, E.J., Behrens, T.E.J., Coalson, T.S., Harms, M.P., Jenkinson, M., Moeller, S., Robinson, E.C., Sotiropoulos, S.N., Xu, J., Yacoub, E., Ugurbil, K., Van Essen, D.C., 2016. The Human Connectome Project's neuroimaging approach. Nature Neuroscience 19, 1175-1187.
Glasser, M.F., Sotiropoulos, S.N., Wilson, J.A., Coalson, T.S., Fischl, B., Andersson, J.L., Xu, J., Jbabdi, S., Webster, M., Polimeni, J.R., Van Essen, D.C., Jenkinson, M., 2013. The minimal preprocessing pipelines for the Human Connectome Project. NeuroImage 80, 105-124.
Halford, G.S., Cowan, N., Andrews, G., 2007. Separating cognitive capacity from knowledge: a new hypothesis. Trends in Cognitive Sciences 11, 236-242.
Harris, T.E., 1964. The theory of branching process. New York: Dover.
He, B.J., 2011. Scale-free properties of the functional magnetic resonance imaging signal during rest and task. The Journal of neuroscience : the official journal of the Society for Neuroscience 31, 13786-13795.
Hearne, L.J., Mattingley, J.B., Cocchi, L., 2016. Functional brain networks related to individual differences in human intelligence at rest. Scientific Reports 6, 32328.
Hesse, J., Gross, T., 2014. Self-organized criticality as a fundamental property of neural systems. Frontiers in systems neuroscience 8, 166-166.
Hobbs, J.P., Smith, J.L., Beggs, J.M., 2010. Aberrant Neuronal Avalanches in Cortical Tissue Removed From Juvenile Epilepsy Patients. Journal of Clinical Neurophysiology 27.
Hu, G., Huang, X., Jiang, T., Yu, S., 2019. Multi-Scale Expressions of One Optimal State Regulated by Dopamine in the Prefrontal Cortex. Frontiers in Physiology 10, 113-113.
Jaeggi, S.M., Buschkuehl, M., Jonides, J., Perrig, W.J., 2008. Improving fluid intelligence with training on working memory. Proceedings of the National Academy of Sciences 105, 6829.

Jung, R.E., Haier, R.J., 2007. The Parieto-Frontal Integration Theory (P-FIT) of intelligence: Converging neuroimaging evidence. Behavioral and Brain Sciences 30, 135-154.

Kanders, K., Lee, H., Hong, N., Nam, Y., Stoop, R., 2020. Fingerprints of a second order critical line in developing neural networks. Communications Physics 3, 13.

Kanders, K., Lorimer, T., Stoop, R., 2017. Avalanche and edge-of-chaos criticality do not necessarily co-occur in neural networks. Chaos: An Interdisciplinary Journal of Nonlinear Science 27, 047408.

Kane, M.J., Engle, R.W., 2002. The role of prefrontal cortex in working-memory capacity, executive attention, and general fluid intelligence: An individual-differences perspective. Psychonomic Bulletin & Review 9, 637-671.

Karahanoğlu, F.I., Van De Ville, D., 2017. Dynamics of large-scale fMRI networks: Deconstruct brain activity to build better models of brain function. Current Opinion in Biomedical Engineering 3, 28-36.

Krienen, F.M., Yeo, B.T.T., Buckner, R.L., 2014. Reconfigurable task-dependent functional coupling modes cluster around a core functional architecture. Philosophical transactions of the Royal Society of London. Series B, Biological sciences 369, 20130526.

Lee, H., Golkowski, D., Jordan, D., Berger, S., Ilg, R., Lee, J., Mashour, G.A., Lee, U., Avidan, M.S., Blain-Moraes, S., Golmirzaie, G., Hardie, R., Hogg, R., Janke, E., Kelz, M.B., Maier, K., Mashour, G.A., Maybrier, H., McKinstry-Wu, A., Muench, M., Ochroch, A., Palanca, B.J.A., Picton, P., Schwarz, E.M., Tarnal, V., Vanini, G., Vlisides, P.E., 2019. Relationship of critical dynamics, functional connectivity, and states of consciousness in large-scale human brain networks. Neuroimage 188, 228-238.

Lei, Y., Song, B., Chen, L., Su, J., Zhang, X., Ni, W., Yu, Y., Xu, B., Yu, L., Gu, Y., Mao, Y., 2020. Reconfigured functional network dynamics in adult moyamoya disease: a resting-state fMRI study. Brain Imaging and Behavior 14, 715-727.

Lidow, M.S., Koh, P.-O., Arnsten, A.F.T., 2003. D1 dopamine receptors in the mouse prefrontal cortex: Immunocytochemical and cognitive neuropharmacological analyses. Synapse 47, 101-108.

Liu, T.T., Nalci, A., Falahpour, M., 2017. The global signal in fMRI: Nuisance or Information? Neuroimage 150, 213-229.

Makris, N., Goldstein, J.M., Kennedy, D., Hodge, S.M., Caviness, V.S., Faraone, S.V., Tsuang, M.T., Seidman, L.J., 2006. Decreased volume of left and total anterior insular lobule in schizophrenia. Schizophrenia Research 83, 155-171.

Marshall, N., Timme, N.M., Bennett, N., Ripp, M., Lautzenhiser, E., Beggs, J.M., 2016. Analysis of Power Laws, Shape Collapses, and Neural Complexity: New Techniques and MATLAB Support via the NCC Toolbox. Frontiers in Physiology 7, 250.

Meisel, C., Olbrich, E., Shriki, O., Achermann, P., 2013. Fading Signatures of Critical Brain Dynamics during Sustained Wakefulness in Humans. The Journal of Neuroscience 33, 17363.

Meisel, C., Storch, A., Hallmeyer-Elgner, S., Bullmore, E., Gross, T., 2012. Failure of Adaptive Self-Organized Criticality during Epileptic Seizure Attacks. PLOS Computational Biology 8, e1002312.

Nakagawa, T.T., Jirsa, V.K., Spiegler, A., McIntosh, A.R., Deco, G., 2013. Bottom up modeling of the connectome: Linking structure and function in the resting brain and their changes in aging. Neuroimage 80, 318-329.

Nikolaidis, A., Baniqued, P.L., Kranz, M.B., Scavuzzo, C.J., Barbey, A.K., Kramer, A.F., Larsen, R.J., 2017. Multivariate Associations of Fluid Intelligence and NAA. Cerebral Cortex 27, 2607-2616.

Omidvarnia, A., Zalesky, A., Van De Ville, D., Jackson, G.D., Pedersen, M., 2019. Temporal complexity of fMRI is reproducible and correlates with higher order cognition. bioRxiv, 770826.

Palva, J.M., Zhigalov, A., Hirvonen, J., Korhonen, O., Linkenkaer-Hansen, K., Palva, S., 2013. Neuronal long-range temporal correlations and avalanche dynamics are correlated with behavioral scaling laws. Proc Natl Acad Sci U S A 110, 3585-3590.

Plenz, D., 2012. Neuronal avalanches and coherence potentials. The European Physical Journal Special Topics 205, 259-301.

Poil, S.-S., Hardstone, R., Mansvelder, H.D., Linkenkaer-Hansen, K., 2012. Critical-State Dynamics of Avalanches and Oscillations Jointly Emerge from Balanced Excitation/Inhibition in Neuronal Networks. The Journal of Neuroscience 32, 9817.

Popiel, N.J.K., S.; Abeyasinghe, P.M.; Riganello, F.; Nichols, E.S.; Owen, A.M.; Soddu, A., 2020. The Emergence of Integrated Information, Complexity, and 'Consciousness' at Criticality. Entropy 22.

Prichard, D., Theiler, J., 1994. Generating surrogate data for time series with several simultaneously measured variables. Physical Review Letters 73, 951-954.

Priesemann, V., Wibral, M., Valderrama, M., Pröpper, R., Le Van Quyen, M., Geisel, T., Triesch, J., Nikolić, D., Munk, M.H.J., 2014. Spike avalanches in vivo suggest a driven, slightly subcritical brain state. Frontiers in systems neuroscience 8, 108-108.

Reinhart, R.M.G., Nguyen, J.A., 2019. Working memory revived in older adults by synchronizing rhythmic brain circuits. Nature Neuroscience 22, 820-827.

Sakoğlu, Ü., Pearlson, G.D., Kiehl, K.A., Wang, Y.M., Michael, A.M., Calhoun, V.D., 2010. A method for evaluating dynamic functional network connectivity and task-modulation: application to schizophrenia. Magnetic Resonance Materials in Physics, Biology and Medicine 23, 351-366.

Saxe, G.N., Calderone, D., Morales, L.J., 2018. Brain entropy and human intelligence: A resting-state fMRI study. PLoS One 13, e0191582.

Scarpetta, S., Apicella, I., Minati, L., de Candia, A., 2018. Hysteresis, neural avalanches, and critical behavior near a first-order transition of a spiking neural network. Physical Review E 97, 062305.

Scott, G., Fagerholm, E.D., Mutoh, H., Leech, R., Sharp, D.J., Shew, W.L., Knöpfel, T., 2014. Voltage Imaging of Waking Mouse Cortex Reveals Emergence of Critical Neuronal Dynamics. The Journal of Neuroscience 34, 16611.

Sethna, J.P., Dahmen, K.A., Myers, C.R., 2001. Crackling noise. Nature 410, 242-250.

Shew, W.L., Plenz, D., 2012. The Functional Benefits of Criticality in the Cortex. The Neuroscientist 19, 88-100.

Shew, W.L., Yang, H., Petermann, T., Roy, R., Plenz, D., 2009. Neuronal Avalanches Imply Maximum Dynamic Range in Cortical Networks at Criticality. The Journal of Neuroscience 29, 15595.

Shew, W.L., Yang, H., Yu, S., Roy, R., Plenz, D., 2011. Information capacity and transmission are maximized in balanced cortical networks with neuronal avalanches. The Journal of neuroscience : the official journal of the Society for Neuroscience 31, 55-63.

Shriki, O., Alstott, J., Carver, F., Holroyd, T., Henson, R.N.A., Smith, M.L., Coppola, R., Bullmore, E., Plenz, D., 2013. Neuronal avalanches in the resting MEG of the human brain. The Journal of neuroscience : the official journal of the Society for Neuroscience 33, 7079-7090.

Smith, S.M., Nichols, T.E., Vidaurre, D., Winkler, A.M., Behrens, T.E.J., Glasser, M.F., Ugurbil, K., Barch, D.M., Van Essen, D.C., Miller, K.L., 2015. A positive-negative mode of population covariation links brain connectivity, demographics and behavior. Nature Neuroscience 18, 1565-1567.

Smyser, C.D., Snyder, A.Z., Shimony, J.S., Mitra, A., Inder, T.E., Neil, J.J., 2016. Resting-State Network Complexity and Magnitude Are Reduced in Prematurely Born Infants. Cerebral cortex (New York, N.Y. : 1991) 26, 322-333.

Solovey, G., Miller, K., Ojemann, J., Magnasco, M., Cecchi, G., 2012. Self-Regulated Dynamical Criticality in Human ECoG. Frontiers in Integrative Neuroscience 6, 44.

Song, B., Ma, N., Liu, G., Zhang, H., Yu, L., Liu, L., Zhang, J., 2019. Maximal flexibility in dynamic functional connectivity with critical dynamics revealed by fMRI data analysis and brain network modelling. Journal of Neural Engineering 16, 056002.

Sotiropoulos, S.N., Jbabdi, S., Xu, J., Andersson, J.L., Moeller, S., Auerbach, E.J., Glasser, M.F., Hernandez, M., Sapiro, G., Jenkinson, M., Feinberg, D.A., Yacoub, E., Lenglet, C., Van Essen, D.C., Ugurbil, K., Behrens, T.E.J., Consortium, W.U.-M.H., 2013. Advances in diffusion MRI acquisition and processing in the Human Connectome Project. Neuroimage 80, 125-143.

Sporns, O., 2013. Network attributes for segregation and integration in the human brain. Current Opinion in Neurobiology 23, 162-171.

Tagliazucchi, E., Balenzuela, P., Fraiman, D., Chialvo, D., 2012. Criticality in Large-Scale Brain fMRI Dynamics Unveiled by a Novel Point Process Analysis. Frontiers in Physiology 3, 15.

Tagliazucchi, E., Chialvo, D.R., 2013. Brain complexity born out of criticality. AIP Conference Proceedings 1510, 4-13.

Tagliazucchi, E., Chialvo, D.R., Siniatchkin, M., Amico, E., Brichant, J.-F., Bonhomme, V., Noirhomme, Q., Laufs, H., Laureys, S., 2016. Large-scale signatures of unconsciousness are consistent with a departure from critical dynamics. Journal of the Royal Society, Interface 13, 20151027-20151027.

Timme, N.M., Marshall, N.J., Bennett, N., Ripp, M., Lautzenhiser, E., Beggs, J.M., 2016. Criticality Maximizes Complexity in Neural Tissue. Frontiers in Physiology 7, 425-425.

Tononi, G., Edelman, G.M., Sporns, O., 1998. Complexity and coherency: integrating information in the brain. Trends in Cognitive Sciences 2, 474-484.

Tononi, G., Sporns, O., Edelman, G.M., 1994. A measure for brain complexity: relating functional segregation and integration in the nervous system. Proceedings of the National Academy of Sciences 91, 5033.

Touboul, J., Destexhe, A., 2010. Can power-law scaling and neuronal avalanches arise from stochastic dynamics? PLoS One 5, e8982-e8982.

Van Essen, D.C., Smith, S.M., Barch, D.M., Behrens, T.E.J., Yacoub, E., Ugurbil, K., Consortium, W.U.-M.H., 2013. The WU-Minn Human Connectome Project: an overview. Neuroimage 80, 62-79.

Vijayraghavan, S., Wang, M., Birnbaum, S.G., Williams, G.V., Arnsten, A.F.T., 2007. Inverted-U dopamine D1 receptor actions on prefrontal neurons engaged in working memory. Nature Neuroscience 10, 376-384.

Wang, B., Niu, Y., Miao, L., Cao, R., Yan, P., Guo, H., Li, D., Guo, Y., Yan, T., Wu, J., Xiang, J., Zhang, H., 2017. Decreased Complexity in Alzheimer's Disease: Resting-State fMRI Evidence of Brain Entropy Mapping. Frontiers in aging neuroscience 9, 378-378.

Wang, R., Lin, P., Liu, M., Wu, Y., Zhou, T., Zhou, C., 2019. Hierarchical Connectome Modes and Critical State Jointly Maximize Human Brain Functional Diversity. Physical Review Letters 123, 038301.

Wendelken, C., Nakhabenko, D., Donohue, S.E., Carter, C.S., Bunge, S.A., 2007. “Brain Is to Thought as Stomach Is to ??”: Investigating the Role of Rostrolateral Prefrontal Cortex in Relational Reasoning. Journal of Cognitive Neuroscience 20, 682-693.

Xia, M., Wang, J., He, Y., 2013. BrainNet Viewer: A Network Visualization Tool for Human Brain Connectomics. PLoS One 8, e68910.

Yang, H., Shew, W.L., Roy, R., Plenz, D., 2012. Maximal Variability of Phase Synchrony in Cortical Networks with Neuronal Avalanches. The Journal of Neuroscience 32, 1061.

Yao, Y., Lu, W.L., Xu, B., Li, C.B., Lin, C.P., Waxman, D., Feng, J.F., 2013. The Increase of the Functional Entropy of the Human Brain with Age. Scientific Reports 3, 2853.

Yeh, F.-C., Liu, L., Hitchens, T.K., Wu, Y.L., 2017. Mapping immune cell infiltration using restricted diffusion MRI. Magnetic Resonance in Medicine 77, 603-612.

Yeh, F.-C., Tseng, W.-Y.I., 2011. NTU-90: A high angular resolution brain atlas constructed by q-space diffeomorphic reconstruction. Neuroimage 58, 91-99.

Yeh, F.-C., Verstynen, T.D., Wang, Y., Fernández-Miranda, J.C., Tseng, W.-Y.I., 2013. Deterministic Diffusion Fiber Tracking Improved by Quantitative Anisotropy. PLoS One 8, e80713.

Yeh, F., Wedeen, V.J., Tseng, W.I., 2010. Generalized q-Sampling Imaging. IEEE Transactions on Medical Imaging 29, 1626-1635.

Zahrt, J., Taylor, J.R., Mathew, R.G., Arnsten, A.F., 1997. Supranormal stimulation of D1 dopamine receptors in the rodent prefrontal cortex impairs spatial working memory performance. The Journal of neuroscience : the official journal of the Society for Neuroscience 17, 8528-8535.

Zalesky, A., Fornito, A., Harding, I.H., Cocchi, L., Yücel, M., Pantelis, C., Bullmore, E.T., 2010. Whole-brain anatomical networks: Does the choice of nodes matter? Neuroimage 50, 970-983.

Zapperi, S., Lauritsen, K.B., Stanley, H.E., 1995. Self-Organized Branching Processes: Mean-Field Theory for Avalanches. Physical Review Letters 75, 4071-4074.